Remote Sensing of Environment 168 (2015) 146–162

Contents lists available at ScienceDirect

Remote Sensing of Environment

journal homepage: www.elsevier.com/locate/rse

SMOS soil moisture assimilation for improved hydrologic simulation in the Murray Darling Basin, Australia

H. Lievens [a,*], S.K. Tomer [b], A. Al Bitar [b], G.J.M. De Lannoy [c], M. Drusch [d], G. Dumedah [e], H.-J. Hendricks Franssen [f], Y.H. Kerr [b], B. Martens [a], M. Pan [g], J.K. Roundy [h], H. Vereecken [f], J.P. Walker [e], E.F. Wood [g], N.E.C. Verhoest [a], V.R.N. Pauwels [e]

[a] Laboratory of Hydrology and Water Management, Ghent University, Ghent, Belgium
[b] Centre d'Etudes Spatiales de la Biosphère, Toulouse, France
[c] Global Modeling and Assimilation Office, NASA Goddard Space Flight Center, Greenbelt, MD, USA
[d] European Space Agency, Noordwijk, The Netherlands
[e] Department of Civil Engineering, Monash University, Victoria, Australia
[f] Forschungszentrum Jülich, Jülich, Germany
[g] Land Surface Hydrology Group, Princeton University, Princeton, NJ, USA
[h] Hydrological Sciences Branch, NASA Goddard Space Flight Center, Greenbelt, MD, USA

ARTICLE INFO

Article history:
Received 21 October 2014
Received in revised form 8 June 2015
Accepted 27 June 2015
Available online xxxx

Keywords:
SMOS
Data assimilation
Soil moisture
Streamflow
Murray Darling Basin

ABSTRACT

This study explores the benefits of assimilating SMOS soil moisture retrievals for hydrologic modeling, with a focus on soil moisture and streamflow simulations in the Murray Darling Basin, Australia. In this basin, floods occur relatively frequently and initial catchment storage is known to be key to runoff generation. The land surface model is the Variable Infiltration Capacity (VIC) model. The model is calibrated using the available streamflow records of 169 gauge stations across the Murray Darling Basin. The VIC soil moisture forecast is sequentially updated with observations from the SMOS Level 3 CATDS (Centre Aval de Traitement des Données SMOS) soil moisture product using the Ensemble Kalman filter. The assimilation algorithm accounts for the spatial mismatch between the model (0.125°) and the SMOS observation (25 km) grids. Three widely-used methods for removing bias between model simulations and satellite observations of soil moisture are evaluated. These methods match the first, second and higher order moments of the soil moisture distributions, respectively. In this study, the first order bias correction, i.e. the rescaling of the long term mean, is the recommended method. Preserving the observational variability of the SMOS soil moisture data leads to improved soil moisture updates, particularly for dry and wet conditions, and enhances initial conditions for runoff generation. Second or higher order bias correction, which includes a rescaling of the variance, decreases the temporal variability of the assimilation results. In comparison with in situ measurements of OzNet, the assimilation with mean bias correction reduces the root mean square error (RMSE) of the modeled soil moisture from 0.058 m^3/m^3 to 0.046 m^3/m^3 and increases the correlation from 0.564 to 0.714. These improvements in antecedent wetness conditions further translate into improved predictions of associated water fluxes, particularly runoff peaks. In conclusion, the results of this study clearly demonstrate the merit of SMOS data assimilation for soil moisture and streamflow predictions at the large scale.

1. Introduction

It is well known that soil moisture (SM) plays a crucial role in the hydrologic cycle, particularly in the partitioning of the incoming radiation into latent and sensible heat fluxes, and in the partitioning of precipitation into surface runoff and infiltration. Given the importance of soil moisture in Earth system processes, a large amount of research has been devoted to the estimation of this variable at large spatial scales through satellite remote sensing. Examples of relevant microwave-based satellite missions for soil moisture monitoring are the Advanced Microwave Scanning Radiometer for Earth observation science (AMSR-E) (Njoku, Jackson, Lakshmi, Chan, & Nghiem, 2003), the Advanced Microwave Scanning Radiometer-2 (AMSR2) (Imaoka et al., 2010), the Soil Moisture Ocean Salinity (SMOS) mission (Kerr et al., 2001), the Advanced Scatterometer (ASCAT) (Wagner et al., 2013), and the Soil Moisture Active Passive (SMAP) mission (Entekhabi et al., 2010).

Another fundamentally different way to obtain information on the surface SM content is by the application of physically-based spatially distributed land surface models (LSMs). These models simulate processes related to the water and energy balance at the land surface. Some well-known examples of such models are the Community Land Model

* Corresponding author.
E-mail address: Hans.Lievens@UGent.be (H. Lievens).

(CLM) (Lawrence et al., 2011), the Variable Infiltration Capacity (VIC) model (Liang, Lettenmaier, Wood, & Burges, 1994; Liang, Wood, & Lettenmaier, 1996, 1999), the Joint UK Land Environment Simulator (JULES) (Best et al., 2011; Clark et al., 2011), and the land and ocean surface platform for coupled or offline simulation of Earth surface variables and fluxes (SURFEX) (Masson et al., 2013).

Even though both remote sensing and hydrologic modeling are very useful for the estimation of spatially distributed SM fields, their estimates remain prone to a significant amount of uncertainty and errors. In the case of remote sensing, these are caused by instrument errors, uncertainties in representativeness, uncertainties in the retrieval algorithm, and Radio Frequency Interference (RFI) (Al Bitar et al., 2012; Choudhury, Schmugge, Chang, & Newton, 1979; Leroux, Kerr, Richaume, & Fieuzal, 2013; Martens, Lievens, Colliander, Jackson, & Verhoest, 2015 Panciera, Walker, & Merlin, 2009; Parrens, Calvet, de Rosnay, & Decharme, 2014; Rahmoune, Ferrazzoli, Kerr, & Richaume, 2013; Sabater, De Rosnay, & Balsamo, 2011; Wang, Oneil, Jackson, & Engman, 1983; Wigneron et al., 2004). In the case of hydrologic models, these errors are caused by uncertainties in parameters, meteorological forcings, land cover, soil texture and topographic data, and conceptual errors or oversimplifications in the model physics (Pauwels, Hoeben, Verhoest, & De Troch, 2001). By combining hydrologic model predictions with remote sensing observations, improved estimates of soil moisture can be expected at large scales (Lahoz & De Lannoy, 2014). Several studies have shown how improvements in antecedent soil moisture conditions after assimilating microwave remote sensing observations may impact the forecasting of runoff (Brocca et al., 2010, 2012; Draper, Mahfouf, Calvet, Martin, & Wagner, 2011; Matgen et al., 2012; Pauwels, Hoeben, Verhoest, De Troch, & Troch, 2002; Pauwels et al., 2001). However, these studies were mainly focused toward active sensors (e.g. ERS and ASCAT) and predictions for small basins. Only few studies have demonstrated the potential of coarse-scale passive microwave observations to improve streamflow predictions of large catchments (Wanders, Karssenberg, de Roo, de Jong, & Bierkens, 2014).

The assimilation of global satellite SM retrievals into hydrologic models presents a number of important challenges. As noted by Wood et al. (2011), it can be expected that LSMs will be applied at fine spatial resolutions, while the remote sensing products will be delivered at significantly coarser spatial resolutions. Either the data assimilation algorithm will have to take into account this spatial mismatch (Sahoo, De Lannoy, Reichle, & Houser, 2013), or the satellite products will have to be pre-processed so their spatial resolution matches the spatial resolution of the hydrologic model (Merlin, Al Bitar, Walker, & Kerr, 2010; Verhoest et al., 2015). Another challenge is the fact that model simulations and satellite retrievals often exhibit differences in SM climatology, i.e. a different long term mean (or bias) and dynamic range (Reichle, Koster, Dong, & Berg, 2004). This may for instance be attributed to the fact that radiometer observations generally have a coarser horizontal (10 to 40 km) and shallower vertical (less than 5 cm) spatial extent compared to models (Sahoo et al., 2013; Wilker, Drusch, Seuffert, & Simmer, 2006). In addition, LSMs may be optimized toward the simulation of streamflow or land-atmosphere fluxes, rather than SM representation (Koster et al., 2009). Other reasons may relate to approximations and shortcomings in both the retrieval algorithms and land surface models (De Lannoy, Houser, Pauwels, & Verhoest, 2007). However, mitigating these climatologic differences between model simulations and observations of SM is necessary for successful data assimilation (De Lannoy et al., 2007; Reichle & Koster, 2004; Kumar et al., 2012).

The objective of this study is to evaluate whether the assimilation of coarse-scale SMOS observations can improve the simulation of soil moisture and streamflow at a finer spatial resolution. Therefore, a data assimilation algorithm is implemented, which resolves the mismatch in horizontal spatial scale through embedding the SMOS antenna pattern weighting function in the observation operator. Furthermore, given its major influence in data assimilation, three widely-used methods for bias mitigation are evaluated. These respectively match (1) only the first order moment (mean), (2) the first and second order moments (mean and variance) and (3) all order moments (including the mean, variance and skewness) of the SM observations to the simulations. Finally, the skill of the data assimilation is validated by comparing soil moisture and streamflow simulations for the period 2010–2011 with measurements of 49 in situ soil moisture stations and 169 gauge stations within the Murray Darling Basin, Australia.

2. Data and methods

2.1. The study site

The Murray Darling Basin (Fig. 1) is one of the world's largest river systems with a drainage area of approximately 1 million km^2, or 14% of the Australian continent. The basin is exposed to a semi-arid climate. Despite the relatively low precipitation and streamflow that dominates the basin, it has been the subject of significant flooding over past years. Floods in the basin are often related to heavy rainfall events, and impacted by antecedent soil moisture conditions. The Murray Darling Basin is one of the most intensive agricultural areas in Australia, accounting for approximately 40% of Australia's total food production. The basin is also extensively monitored for soil moisture, precipitation and streamflow, thus making it an ideal test-bed for the validation of hydrologic model and data assimilation systems.

Soil moisture measurements were available from the Murrumbidgee Soil Moisture Monitoring Network (OzNet), which consists of 62 stations located across the 82,000 km^2 Murrumbidgee River Catchment, a sub-basin in the Southeast of the Murray Darling Basin (Smith et al., 2012). The data were quality-assured conform to Su, Ryu, Young, Western, and Wagner (2013), after which 49 in situ sites were retained (Fig. 1). The stations are all located within grassland or cropland areas, and equipped with a mixture of time-domain interferometer-based Campbell Scientific probes measuring the 0–8 cm topsoil, and Stevens Hydraprobes measuring the 0–5 cm topsoil. In order to compare with the model simulations, the in situ measurements of the different stations were processed to hourly values and aggregated by averaging per 0.125° VIC grid cell. As a result, 21 different pixels with hourly in situ soil moisture measurements were obtained. Measurements were available from the start of 2010 to September 2011. A detailed description of the in situ stations can be found in Su et al. (2013).

Daily streamflow records have been collected for 169 gauge stations, which are mainly located along the East boundary of the basin (Fig. 1). The stations are maintained by three organizations: the Murray Darling Basin Authority (MDBA), the Department of Environment and Resource Management (DERM) in Queensland, and the New South Wales Office of Water (NOW). The data have been collected and provided through the Australian Bureau of Meteorology, and contain daily water heights (m) and streamflow (10^3 m^3/day) measurements from 2005 to 2011. Also metadata of the stations were available, including the geographic positions of the stations, an indication of possible dam impacts on streamflow, and the drainage area (km^2). Note that the drainage area for the available stations ranges between 50 km^2 to 80,000 km^2, with an average of 3400 km^2. The stations prone to dam regulations were removed from the data set, as such regulation was not included in the hydrologic model.

2.2. The land surface model

The Variable Infiltration Capacity (VIC) model (Liang et al., 1994, 1996, 1999) is a distributed LSM that accounts for both the water and energy budgets. During the last decades, the VIC model has been widely-used in a number of applications (Maurer, O'Donnell, Lettenmaier, & Roads, 2001; Nijssen, Schnur, & Lettenmaier, 2001; Sheffield et al., 2003; Sheffield & Wood, 2008). The grid cell size of VIC can be specified between 1 km and hundreds of kilometers, where each cell can be statistically subdivided into fractions that represent different land cover types.

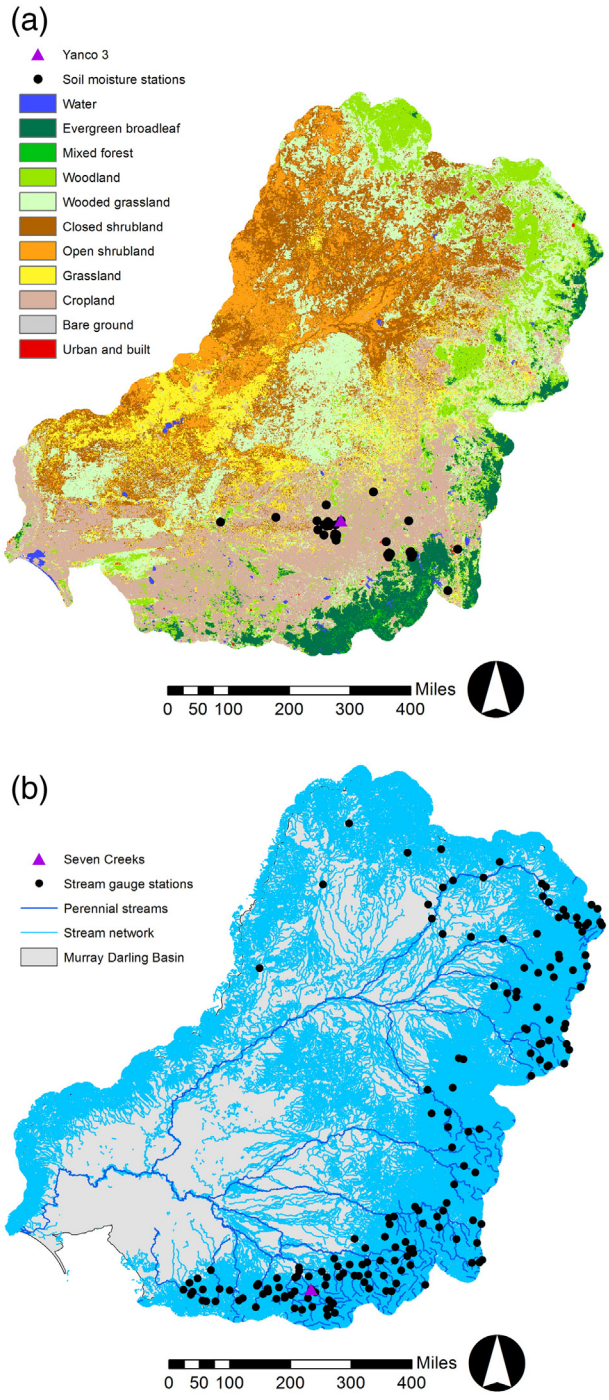

Fig. 1. The (a) land cover and (b) stream network for the Murray Darling Basin, Australia. The locations of the soil moisture in situ stations (OzNet) are shown in (a), whereas the locations of the stream gauge stations are shown in (b). The focus sites for this study, i.e. Yanco 3 for soil moisture and Seven Creeks for streamflow are highlighted in magenta.

The present study uses a grid spacing of 0.125° by 0.125°, which approximately corresponds to 12.5 km by 12.5 km.

Associated with each land cover type is a single canopy layer, and three soil layers. The canopy layer determines the interception of precipitation as a function of leaf area index (LAI) according to a biosphere–atmosphere transfer scheme (BATS) (Dickinson, Henderson-Sellers, Kennedy, & Wilson, 1986). The first soil layer represents the top 10 cm, whereas the second and third layer depths are variable. The first two layers control the partitioning of precipitation into surface runoff and infiltration, hence, they capture the dynamic response to the infiltrated precipitation. Thereby, diffusion of soil moisture is allowed in case of a wetter second layer. The infiltration capacity i is given by the Variable Infiltration Capacity curve (Zhao, Zang, Fang, Liu, & Zhang, 1980):

$$i = i_m\left[1-(1-A)^{1/b}\right], \tag{1}$$

where i_m is the maximum infiltration capacity, A is the fraction of area for which the infiltration is less than i, and b is a shape parameter. The third layer receives moisture from the second layer through gravity drainage, with a hydraulic conductivity given by the Brooks–Corey relationship for unsaturated soils (Brooks & Corey, 1964), and controls the generation of baseflow through a nonlinear recession curve.

2.2.1. Input data

The simulations make use of the MERRA (Modern-Era Retrospective Analysis for Research and Applications) forcing data set (Rienecker et al., 2011). Seven meteorological forcing fields were processed at an hourly time step: precipitation, 2-meter air temperature, pressure, vapor pressure, wind speed, and incoming shortwave and longwave radiation. The forcing data were initially provided on a 1/2° latitude by 2/3° longitude grid with hourly temporal coverage from 2005 to 2011, and were reprocessed by nearest neighbor resampling on the 0.125° VIC grid. The precipitation field has been further corrected to match the Bureau of Meteorology – Australian Water Availability Project (BAWAP) observations (Jones, Wang, & Fawcett, 2009) on monthly time scales. The BAWAP precipitation is a local daily product with 5-km spatial resolution, based on gauge data. Prior to this bias correction, the BAWAP data were upscaled to the MERRA grid by weighted averaging, with weights depending on the spatial coverage. Subsequently, the MERRA precipitation was corrected by multiplying each hourly cell by the ratio of the monthly BAWAP over MERRA fields. For regions where BAWAP observations were lacking, the MERRA precipitation was left uncorrected.

The soil input data were provided through the CSIRO (Commonwealth Scientific and Industrial Research Organisation) Land and Water and are based on the Australian Soil Resource Information System (ASRIS) (McKenzie, Jacquier, Maschmedt, Griffin, & Brough, 2012). The soil variables comprise of texture (sand and clay content), bulk density, and saturated hydraulic conductivity. Land cover data were extracted from the global 1-km University of Maryland (UMD) data set (Hansen, Defries, Townshend, & Sohlberg, 2000), based on which the sub-grid vegetation fractions were calculated for the coarser 0.125° model grids. The LAI was sourced from the level-4 MOD15A2 MODIS (Moderate Resolution Imaging Spectroradiometer) Terra product (Knyazikhin et al., 1999). This global MODIS LAI product is composited every 8 days at 1 km resolution on a sinusoidal grid. The original data were reprocessed in order to extract climatological monthly LAI for each land cover tile per 0.125° grid cell.

2.2.2. Model calibration

A calibration algorithm was applied to optimize the VIC simulations of streamflow based on measurements of the 169 unregulated gauge stations across different sub-basins of the Murray Darling Basin. The method applied is entirely adopted from Troy, Wood, and Sheffield (2008) and makes use of the Shuffled Complex Evolution (SCE-UA) optimization algorithm (Duan, Sorooshian, & Gupta, 1992, 1994). The model calibration was performed based on data from the start of 2005 to the end of 2010. The validation of the model and data assimilation experiments was performed for the period 2010–2011. Thus, the year 2010 is included both in the calibration and validation period. This was necessary as (1) the Southeast of Australia experienced a large drought during 2000–2009 such that the inclusion of 2010 in the calibration period ensured a better representation of wet conditions, and (2) most of the soil moisture and streamflow measurements are only

available for a part of 2011 such that the inclusion of 2010 was necessary to increase the robustness of the validation.

The model parameters selected for the calibration were *b*, *Ds*, *Dsmax*, *Ws*, *dp*2 and *dp*3, as recommended by previous calibration studies with VIC (Troy et al., 2008). Table 1 shows a description of the calibration parameters and their allowed range. Unlike typical calibration methods, which assume lumped parameters (i.e. every grid in the catchment has the same parameters), the method of Troy et al. (2008) calibrates each grid cell in the catchment separately. This is advantageous over a lumped method as it provides spatial variability in the parameters. A disadvantage of this method is that it requires an observation of gridded runoff in order to calibrate each grid cell. This gridded runoff observation can be estimated by assuming a constant runoff ratio throughout the catchment and using the spatial variability of precipitation to derive the gridded runoff field. However, due to the time lag between precipitation and gauge runoff, it is only applicable at time steps larger than a month (Troy et al., 2008). Hence, the calibration is limited to a monthly time scale. Note that the use of monthly forecasts also circumvents inadvertent uncertainties caused by regulations and the need of a coupled routing scheme during calibration. Nevertheless, after the VIC calibration a linear routing scheme (see Section 2.2.3) was coupled to further improve the characteristics of the sub-monthly (daily) simulations. As it is based on gridded runoff observations, the method only allows for calibrating grid cells that are located within the drainage area of the 169 selected gauge stations. To obtain full spatial coverage, the parameters for the remaining grid cells of the entire Murray Darling Basin were interpolated using inverse distance weighting. Nevertheless, the performance of the calibration can only be evaluated for the drainage area covered by the selected catchments.

The calibration objective function used to match the performance of the streamflow simulations with observations is the Kling Gupta Efficiency (KGE), introduced by Gupta, Kling, Yilmaz, and Martinez (2009):

$$\mathrm{KGE} = 1 - \sqrt{W_1(1-\mathrm{R})^2 + W_2(1-\mathrm{MR})^2 + W_3(1-\mathrm{SR})^2}, \quad (2)$$

where R is the correlation coefficient between the simulations and observations, MR the ratio between the mean of the simulations and the mean of the observations, and SR the ratio between the standard deviation of the simulations and the standard deviation of the observations. Thus, the KGE simultaneously optimizes for correlation, bias and variability. Note that the optimal value of the three criteria is 1, through which the optimal value of the KGE becomes 1. W_1 to W_3 are weights that can be assigned to specify the relative importance of the different criteria for the problem at hand. In this study, equal weights have been assigned to all three criteria ($W_1 = W_2 = W_3 = 1$).

2.2.3. Routing model

To improve the representation of daily streamflow simulations at the locations of the gauge stations, the VIC model is coupled with a simple off-line linear routing model. The routing model lags the runoff for VIC grids that are located upstream of a specific gauge station. Thereby, the time lag in runoff *L* is introduced as:

$$L = a_r + b_r \Delta x, \quad (3)$$

where Δx denotes the distance between a grid cell and the station along the line of flow direction. The flow directions were taken from the 30 arc-second HydroSHEDS (Hydrological data and maps based on SHuttle Elevation Derivatives at multiple Scales) data set (Lehner, Verdin, & Jarvis, 2006). The parameters a_r and b_r are optimized iteratively for each station drainage area, through iteratively running a large number of combinations and selecting the one with the highest KGE. It should be remarked that the simplistic formulation of the routing model could potentially contribute to errors in the daily streamflow estimation.

Table 1
The calibrated VIC parameters and their allowed range.

Parameter	Range	Description
b (−)	0.01–0.80	Variable infiltration curve shape
Ds (−)	0.00–1.00	Fraction of *Dsmax* where nonlinear baseflow begins
Dsmax (mm/d)	0.10–50.00	Maximum baseflow velocity
Ws (−)	0.10–1.00; *Ws* > *Ds*	Fraction of maximum SM content above which nonlinear baseflow occurs
*dp*2 (m)	0.1–3.0	Thickness of layer 2
*dp*3 (m)	0.1–3.0	Thickness of layer 3

2.3. The SMOS observations

SMOS provides regular (±3-day repeat period) observations of SM at global scale, which are operationally retrieved through the ESA (European Space Agency) Level 2 processor (Kerr et al., 2012). For this study, the SM observations have been extracted over the Murray Darling Basin from January 2010 to December 2011, in accordance with the availability of the forcing and streamflow data, and were sourced from the Level 3 CATDS (Centre Aval de Traitement des Données SMOS) product (Jacquette et al., 2010) version 244 from reprocessing campaign RE01. In essence, the Level 3 algorithm is an extension of the Level 2 product, providing enhanced SM retrievals for individual orbits by employing multi-orbit retrievals of vegetation parameters. The Level 3 CATDS SM is a daily global product, available on a 25 km cylindrical projection over the EASE (Equal Area Scalable Earth) grid. Although the actual resolution of SMOS is about 43 km, Dumedah, Walker, and Rüdiger (2014) have shown that the application of 43 km SMOS data at finer-scale grids (e.g. 15 km or 25 km) is not expected to add substantial error. The vertical sampling depth of the SMOS L-band observations is generally assumed in the order of 2.5–3.5 cm (Escorihuela, Chanzy, Wigneron, & Kerr, 2010).

Besides SM information, the SMOS product contains quality indicators for soil moisture and RFI, as well as science flags indicating the presence of snow, frozen soils, etc. The SMOS observations have been extensively filtered, by removing data when soil or air temperatures (according to the LSM forcings and simulations) are below 2.5 °C, and flags for snow or frozen soils (provided by the European Centre for Medium-Range Weather Forecasts, ECMWF) are activated. Moreover, it is not expected that snow or frozen soil conditions will have an impact on the analysis due to the limited temporal and spatial occurrence in the Murray Darling Basin. Finally, filters have been implemented to exclude data with a probability of RFI larger than 0.2, and urban or water cover fractions larger than 0.1.

The processed (i.e. quality-assured) SMOS retrievals were assimilated into the VIC model at the time of the overpass, which corresponds to 6 am local time for ascending orbits and 6 pm local time for descending orbits.

2.4. The data assimilation algorithm

2.4.1. The Ensemble Kalman filter

The data assimilation uses the Ensemble Kalman Filter (EnKF). A flowchart presenting the different steps in the assimilation scheme is provided in Fig. 2. An extensive description of the EnKF can be found in Evensen (1994). Consequently, only a short description is provided in this paper. The state variables of a single forecast ensemble member are stored in the vector $\mathbf{x}_k^{if}$, where *k* indicates the time step and *i* the ensemble member. The superscript *f* refers to the forecast variables, and thus the variables that are obtained prior to assimilation of the external data. The state variables that are updated in this study are the first and

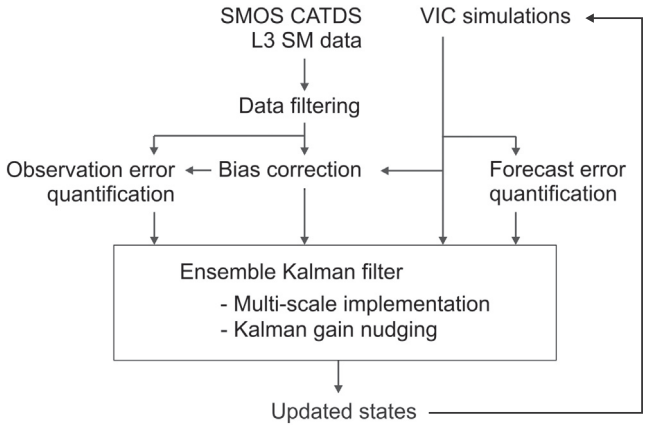

Fig. 2. Flowchart of the data assimilation setup.

second layer SM, in order to enhance the simulations of associated runoff. The third layer SM, associated to baseflow, is not analyzed. The main motivation therefore is that SMOS provides observations of the top surface SM, and hence, is expected to improve the runoff simulation. State variables obtained after the assimilation of the external data are referred to as analyzed variables, and are thus denoted with the superscript *a*. The analyzed state vector at time step $k-1$ is propagated to the next time step using:

$$\mathbf{x}_k^{if} = \mathbf{f}_{k-1}\left(\mathbf{x}_{k-1}^{ia}\right) + \mathbf{w}_{k-1}^{i}, \tag{4}$$

where $\mathbf{f}_{k-1}(.)$ is the model and $\mathbf{w}_{k-1}^{i}$ a realization of the forecast error. The system is observed as:

$$\mathbf{y}_k = \mathbf{h}_k(\mathbf{x}_k, \mathbf{v}_k), \tag{5}$$

with $\mathbf{h}_k(.)$ the nonlinear observation operator, mapping the state variables to observation space, and $\mathbf{v}_k$ the observation error.

An important aspect in data assimilation is the estimation of the uncertainty in the forecasts. In the EnKF, the forecast error covariance is estimated as:

$$\begin{cases} \mathrm{P}_k^f &= \dfrac{1}{N-1}\mathrm{D}_{xk}\mathrm{D}_{xk}^{\mathrm{T}} \\ \mathrm{D}_{xk} &= \left[\mathrm{x}_k^{1f} - \overline{\mathrm{x}}_k^f, \quad \ldots, \quad \mathrm{x}_k^{Nf} - \overline{\mathrm{x}}_k^f\right], \\ \overline{\mathrm{x}}_k^f &= \dfrac{1}{N}\sum_{i=1}^{N}\mathrm{x}_k^{if} \end{cases} \tag{6}$$

where N is the number of ensemble members and superscript T indicates the transpose operator. The Kalman Gain $\mathbf{K}_k$ is then calculated as:

$$\mathbf{K}_k = \mathbf{P}_k^f\mathbf{H}_k^{\mathrm{T}}\left[\mathbf{H}_k\mathbf{P}_k^f\mathbf{H}_k^{\mathrm{T}} + \mathbf{R}_k\right]^{-1}, \tag{7}$$

where $\mathbf{R}_k$ is the observation covariance, and $\mathbf{H}_k$ is the Jacobian of the observation operator $\mathbf{h}_k(.)$. For nonlinear observation systems, the need for the explicit calculation of $\mathbf{H}_k$ can be bypassed by the use of the ensemble statistics:

$$\begin{cases} \mathrm{P}_k^f\mathrm{H}_k^T &= \dfrac{1}{N-1}\mathrm{D}_{xk}\mathrm{D}_{yk}^{\mathrm{T}} \\ \mathrm{H}_k\mathrm{P}_k^f\mathrm{H}_k^T &= \dfrac{1}{N-1}\mathrm{D}_{yk}\mathrm{D}_{\mathrm{yk}}^{\mathrm{T}} \\ \mathrm{D}_{yk} &= \left[\mathrm{y}_k^{1f} - \overline{\mathrm{y}}_k^f, \quad \ldots, \quad \mathrm{y}_k^{Nf} - \overline{\mathrm{y}}_k^f\right]. \\ \overline{\mathrm{y}}_k^f &= \dfrac{1}{N}\sum_{i=1}^{N}\mathrm{y}_k^{if} \end{cases} \tag{8}$$

Pauwels and De Lannoy (2009) clearly showed the better performance of this approach as compared to the explicit calculation of $\mathbf{h}_k(.)$ through linearization of the observation system. Using the Kalman Gain, the states of the individual ensemble members are then updated by:

$$\mathbf{x}_k^{ia} = \mathbf{x}_k^{if} + \mathbf{K}_k\left[\mathbf{y}_k - \mathbf{h}_k\left(\mathbf{x}_k^{if}\right) + \mathbf{v}_k^i\right], \tag{9}$$

where $\mathbf{h}_k(\mathbf{x}_k^{if})$ is the simulation of the observation for ensemble member *i*, frequently written as $\mathbf{y}_k^{if}$. Finally, $\mathbf{v}_k^i$ is a random realization of the observation error.

2.4.2. Multi-scale implementation

As noted in the introduction, a specific problem in the assimilation of coarse-scale satellite data is the mismatch in the spatial resolution of the remote sensing data and the land surface model results. More specifically, the SMOS grid has a 25 km spacing, whereas the model grid is spaced at 0.125°, corresponding roughly to 12.5 km. The data assimilation algorithm needs to take into account this horizontal spatial mismatch. In this study, the SMOS observations are assimilated separately for each SMOS grid cell, which typically covers between 2 and 6 VIC grid cells. Thus, a specific 25 by 25 km SMOS grid cell is only used for updating the underlying model grid cells of which their center falls within the observation cell. We recognize that this approach discards the spatial error correlations between adjacent 25-km observations. Since two soil moisture layers in VIC are updated, the state vector for each SMOS grid can be written as:

$$\mathbf{x}_k^{if} = \left[\theta_{1,1,k}^{if} \;\; \theta_{1,2,k}^{if} \;\; \theta_{2,1,k}^{if} \;\; \ldots \;\; \theta_{M,1,k}^{if} \;\; \theta_{M,2,k}^{if}\right]^{\mathrm{T}}, \tag{10}$$

where $\theta_{m,l,k}^{if}$ stands for the modeled soil moisture for model grid *m* and layer *l* inside each SMOS grid, for time step *k* and ensemble member *i*. *M* stands for the number of VIC grids inside each SMOS grid.

To map the VIC model simulations into the observation space, the model states at 0.125° grid are aggregated to the 25 km SMOS grid through the observation operator. A specific property of microwave remote sensing products is that locations near the grid center contribute somewhat more to the observed signal than locations further away from the grid center as a function of the antenna weighting pattern. The consequence is that, if multiple model grid cells are located inside a SMOS observation, the weights of these model grids in the aggregation of the model results to the SMOS grids will not all be equal. Therefore, this spatial weighting is taken into account in the observation operator:

$$\mathbf{H}_k = [w_1 \;\; 0 \;\; w_2 \;\; 0 \;\; \ldots \;\; w_M 0], \tag{11}$$

where the weights *w* are extracted from the SMOS antenna pattern weighting function (Kerr et al., 2011). The observation prediction of coarse-scale surface soil moisture content is then simply:

$$\mathbf{y}_k^{if} = \mathbf{H}_k\mathbf{x}_k^{if}. \tag{12}$$

The corresponding assimilated observation is in this case simply a scalar, more specifically the remotely sensed SMOS soil moisture value.

2.4.3. Kalman Gain nudging

In VIC, the runoff generation is a function of the total SM content of the first two soil layers. Thereby, layer 1 is designed with a shallow depth (10 cm) to capture the fast dynamic response of the soil to precipitation. Although slightly thicker, the depth of this layer approaches the vertical sample space of the SMOS observations. Conversely, layer 2 has a significantly thicker depth which varies between 10 cm and 3 m, to act as a buffer layer for gravity drainage to the groundwater. Due to its larger layer depth, the SM content of layer 2 dominates the total SM content, and therefore also the runoff generation. To improve the runoff simulations, it is therefore important that the assimilation of surface soil

moisture observations influences the soil moisture content of the deeper soil layer.

Some studies have shown that updating only surface soil moisture during data assimilation may not be sufficient to modify the deeper soil moisture profile accordingly (Houser et al., 1998; Walker, Willgoose, & Kalma, 2001). A simple approach to align the updates of the underlying soil layer is to assume that the ratio of the surface soil moisture to the deep soil moisture remains the same before and after assimilation (Burke, Shuttleworth, Lee, & Bastidas, 2001). Alternatively, a Newtonian nudging assimilation technique can be used to relax the profile soil moisture states toward the observation through accounting for a vertical weighting function (Houser et al., 1998). In the specific case of the EnKF, the deeper soil moisture states inherently respond to the assimilation of a surface soil moisture observation through the state error covariance matrix, and eventually through model propagation (Sahoo et al., 2013).

However, because of the relatively large differences in the first two layer depths of VIC, the error covariances between these layers are very low, and show in many cases negative values. As a consequence of these negative error covariances, the analysis increment for layer 2 SM often shows an opposite sign compared to the increment for layer 1. In other words, a wet (dry) observation of SMOS relative to the first layer SM content may cause an increase (decrease) in layer 1 SM, while decreasing (increasing) the SM of layer 2. As such, the total SM state of layers 1 and 2, and consequently runoff, remains unaltered. Note that similar issues with vertical SM error covariances have been reported previously by Li, Crow, and Kustas (2010); Chen, Crow, Starks, and Moriasi (2011); Brocca et al. (2012). One way to bypass this problem is by artificially inducing vertical correlations through direct perturbation of the SM states (e.g. Chen et al. (2011)). This study presents an alternative method which refrains from perturbing the model states. Instead, a Kalman Gain nudging technique is implemented, similar as is used in Newtonian nudging (Houser et al., 1998). The objective of the nudging is to update the second layer SM of VIC as a fraction of the first layer update. Thus, the Kalman Gain element for layer 2 is calculated as a fraction F of $\mathbf{K}$ for layer 1. The update equation for the state element of layer 2, $\mathbf{x}_{k2}$, then becomes:

$$\mathbf{x}_{k2}^{ia} = \mathbf{x}_{k2}^{if} + F\mathbf{K}_{k1}\left[\mathbf{y}_k - \mathbf{h}_k\left(\mathbf{x}_k^{if}\right) + \mathbf{v}_k^i\right], \tag{13}$$

The fraction F was set to 1 for the entire basin in order to maximize the gain of the assimilation. Recall that due to its larger thickness, the second layer has a dominant influence on runoff. Hence, selecting a lower value for F would considerably decrease the impact. Note that furthermore no assumptions have been made regarding the spatial or temporal variability of F. Finally, as reported by Chen et al. (2011) and Brocca et al. (2012), vertical error covariances have important effects on the efficiency of data assimilation, and are an important subject for further research.

2.4.4. Bias removal

An important pre-requisite to the application of data assimilation is the presence of zero mean, temporally uncorrelated forecast and observation errors (Sahoo et al., 2013). In practice, however, the climatologies of model SM forecasts may deviate from those of remote sensing observations due to differences in representation, e.g. spatial resolution and layer depth (Reichle et al., 2004). Therefore, climatologic differences need to be mitigated prior to assimilating the data to resolve part of the representativeness issues. Some studies attribute bias to either forecast or observation bias, but most studies refrain from attributing climatologic differences to either the model or the observations, rescale the observations to the model climatology and only validate the results in terms of variability (not absolute values), e.g. Reichle and Koster (2004); Drusch, Wood, and Gao (2005); Crow, Koster, Reichle, and Sharif (2005); Kumar et al. (2012).

In this study, three simple and widely-used methods for rescaling the observations prior to data assimilation were applied. These respectively rescale the first order moment (long term mean), the first and second order moments (mean and variance), and all order moments (the distribution). The rescaling is performed on a pixel-by-pixel basis by comparing the corresponding values of aggregated VIC simulations (based on the antenna weighting function) and SMOS observations at ascending (6 am local time) and descending (6 pm local time) time steps for the 2-year period of 2010–2011. Note that ascending and descending orbits are treated separately, as they often reveal different statistics (e.g. due to differences in ionospheric or surface conditions at 6 am/6 pm, or tilt- and azimuth-dependent RFI (Bircher, Skou, Jensen, Walker, & Rasmussen, 2012; Leroux et al., 2014; Lievens et al., 2015; Verhoest et al., 2015)). The minimum number of data pairs (simulations and observations) for application of the bias correction was set to 30. Grid cells with less data were masked during the assimilation. The number of masked cells is 36 for ascending and 9 for descending orbits, which corresponds to approximately 2% and 0.5% of the total number of grid cells within the basin.

The bias in the first order moment (MEAN) was removed by comparing the corresponding pixel-based mean values of the VIC simulations and SMOS observations as:

$$SM^* = \overline{SM}_{\mathrm{sim}} + \left(SM_{\mathrm{obs}} - \overline{SM}_{\mathrm{obs}}\right), \tag{14}$$

with SM^* the rescaled SMOS SM observation, $\overline{SM}_{\mathrm{obs}}$ the 2-year mean of the SM observations, and $\overline{SM}_{\mathrm{sim}}$ the 2-year mean of the SM simulations, aggregated to the SMOS grid using the spatial antenna weighting function. Note that in the rescaling of the mean a cutoff at 0.01 m^3/m^3 was implemented to avoid physically impossible values. Furthermore, the analysis update was bounded at the soil porosity value.

The bias correction accounting for both the first and second order moments (SD) was performed according to (Crow et al., 2005; Kumar et al., 2012; Dumedah & Walker, 2014):

$$SM^* = \overline{SM}_{\mathrm{sim}} + \left(SM_{\mathrm{obs}} - \overline{SM}_{\mathrm{obs}}\right)\frac{\sigma_{\mathrm{sim}}}{\sigma_{\mathrm{obs}}} \tag{15}$$

where σ_{sim} and σ_{obs} are the 2-year temporal standard deviations of the SM simulations and observations, respectively.

The bias correction accounting for all order moments (CDF) was performed through matching the CDF of the observations to the CDF of the simulations. The CDFs were computed using the non-parametric kernel-based method by Li, Sheffield, and Wood (2010). Subsequently, SM observations were rescaled to the distribution of the simulations via their corresponding cumulative probabilities. It should be mentioned, however, that the rescaling of the higher order moments may be sub-optimal given the restricted time span (i.e. 2 years) of the observations for the construction of the CDF.

The selection of the three bias correction methods was based on their simplicity and wide-spread use. However, it should be noted that these techniques have several shortcomings that may lead to sub-optimal bias reduction. For instance, if the signal-to-noise (SNR) ratio differs between the simulations and observations of soil moisture, the rescaling of the variance or CDF-matching of the observations may suppress or inflate the signal variance (Yilmaz & Crow, 2013; Su, Ryu, Crow, & Western, 2014). Furthermore, recent studies have shown the more optimal correction of biases when applied to soil moisture anomaly observations (Albergel et al., 2012) and when applied over multi-temporal scales (Su & Ryu, 2015). Alternatively, bias correction could also be implemented online through estimation within a data assimilation scheme (De Lannoy et al., 2007; Pauwels, De Lannoy, Hendricks Franssen, & Vereecken, 2013). A thorough analysis of more comprehensive bias correction methods, including anomaly corrections and multi-scale analysis in a real data assimilation experiment could be an important subject for future research.

2.4.5. The forecast error

The characterization of the forecast error was based on an ensemble of model runs, where the number of stochastic realizations was set to 32. This number was selected as it has been shown that for a model similar to VIC, there was no gain in increasing the ensemble size beyond 32 (Reichle & Koster, 2003). The ensemble generation was based on the multiplicative perturbation of model forcings and parameters with zero-mean random white noise, with a pre-selected standard deviation (σ). The model forcings that were perturbed are precipitation and shortwave radiation. The perturbed model parameters were the bulk density (which affects soil hydraulic parameters) and the exponent of the Brooks–Corey relationship. The latter parameters have been selected based on a sensitivity analysis, where a large range of parameters were perturbed with σ equal to 0.1 times the parameter value. This allowed for selecting the parameters that had the largest impact on the soil moisture ensemble, and to quantify the magnitude of the impact (data not shown). Table 2 provides a list of the perturbed forcings and parameters and their predefined values for σ.

Spatial correlation has been introduced in both the forcing and parameter perturbations. This ensured the generation of spatially coherent forecast errors, which are physically more realistic. Another important aspect was the fact that the introduction of spatially correlated errors increased the analysis increments. More specifically, spatially correlated forecast errors increase the off-diagonal error covariances, which theoretically increases the Kalman Gain. This can be proven by explicitly writing out the Kalman filter equations. The spatially correlated noise was generated based on a simple auto-regressive model:

$$Z_{x,y} = a_f Z_{x-1,y} + b_f Z_{x,y-1} + ex, y, \tag{16}$$

where x and y are the longitudinal and latitudinal coordinates, respectively. Z is the perturbation noise, a_f and b_f are parameters, and e is a white noise term. Through calculation of the variance of the perturbation, and the autocorrelations with spatial lag 1 in both the x- and y-directions, and by solving the resulting system of equations for the model parameters, the following expressions are obtained:

$$\begin{cases} a_f = \dfrac{\rho}{1+\rho} \\ b_f = \dfrac{\rho}{1+\rho} \\ \sigma_e^2 = \sigma_Z^2 \dfrac{1-3\rho^2+2\rho^3}{1-\rho^2}, \end{cases} \tag{17}$$

where ρ is the autocorrelation with spatial lag 1 (assumed similar in both the x- and y-directions) as defined by the user, σ_e^2 is the variance of the white noise, and σ_Z^2 is the variance of the perturbations. The correlation for the generation of noise was arbitrarily set to 0.5 at lag 1 (i.e. 0.125° distance). Correspondingly, the correlation length (the distance characterized by a correlation equal to $1/e$) lays between one and two 0.125° grid cells.

Fig. 3(a) shows the mean soil moisture forecast error (standard deviation) for the model grid in the Murray Darling Basin for the year 2010. The spatial dynamics in the forecast error are logically affected by the selected perturbation parameters. More specifically, the forecast error is partly driven by the spatial variability in soil parameters, such as the bulk density. Furthermore, it is significantly affected by the spatial variability in precipitation, with larger values over the Great Dividing Range and Australian Alps in the East and Southeast of the basin.

Table 2
The perturbed fields and their standard deviations for the generation of ensembles.

Perturbed field	Standard deviation (−)
Brooks–Corey exponent	0.4
Bulk density	0.1
Shortwave radiation	0.1
Precipitation	0.3

2.4.6. The observation error

The objective of the SMOS mission is to deliver global maps of SM with an accuracy of 0.04 m^3/m^3 (Kerr et al., 2012). One option is to use this target accuracy value to characterize the observation error. However, the actual observation error typically depends on the spatial

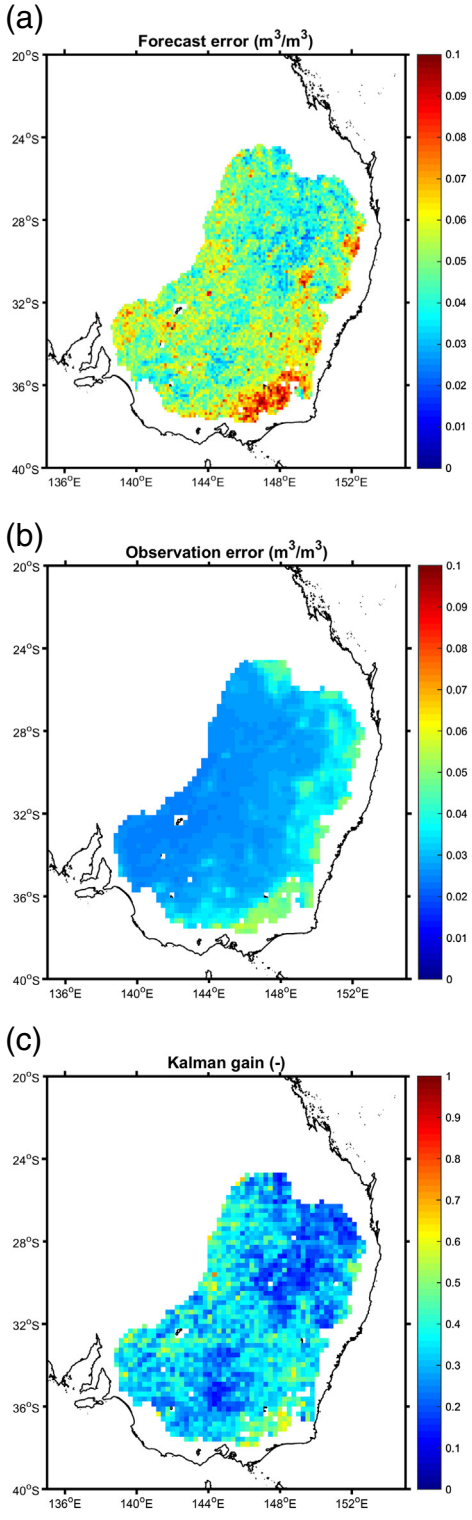

Fig. 3. The 2010 mean soil moisture (a) forecast error over the VIC grid, (b) observation error over the SMOS grid, and (c) Kalman Gain.

location and time of the year (Brocca et al., 2012). For instance, dense vegetation obscures the emitted radiance of the soil surface, through which a larger uncertainty will be associated to the surface SM retrievals. Furthermore, the observation error is time-variant, e.g. due to the variable performance of the retrieval model, which for instance depends on the number of multi-incidence observations, and variation in the vegetation water content, etc. This study proposes the following model for the characterization of the observation error standard deviation:

$$\sigma_R = a_o + b_o \mathrm{DQX} + c_o \mathrm{FFO}, \tag{18}$$

where DQX (m^3/m^3) is the soil moisture retrieval convergence (Kerr et al., 2011), which gives an indication of uncertainty for the soil moisture estimate, irrespective of representativeness errors (e.g. errors caused by vegetation or different layer depths, i.e. 10 cm model depth versus <5 cm retrieval depth). The representativeness errors are accounted for by the parameter a_o, which represents the minimum retrieval error, and the FFO (−), which is the fraction of the SMOS grid cell covered by forest. The parameters a_o, b_o and c_o can be defined by the user. For this study, the parameter values were $a_o = 0.02$, $b_o = 0.5$ and $c_o = 0.02$. This means that the minimum observation error equals 0.02 m^3/m^3, and increases with decreased convergence of the soil moisture retrieval (DQX) and increased forest coverage (FFO). The DQX ranges from close to zero to 0.07 m^3/m^3, whereas the FFO ranges from 0 to 1. Hence, for the described set of parameters, the observation error ranges from 0.02 to a maximum value of 0.075 m^3/m^3. The latter range corresponds well to estimates of the soil moisture retrieval error based on in situ stations in Southeast Australia (Su et al., 2013). For a large number of in situ stations within the Murrumbidgee Basin, bias-free retrieval errors (Root Mean Square Differences) were estimated from approximately 0.02 m^3/m^3 to 0.1 m^3/m^3, with an average of 0.049 m^3/m^3 for ascending and 0.043 m^3/m^3 for descending orbits. It should be mentioned that the selected parameters for the observation error characterization provide only first guess recommendations, which have not been thoroughly optimized with respect to the performance of the assimilation. A thorough optimization of the observation error could be an interesting subject for further research.

Note that the model could potentially be further extended to include uncertainty information related to RFI and/or contributions from open water surfaces, which were highlighted by Al Bitar et al. (2012); Leroux et al. (2013) as major error sources in the SMOS retrievals. However, this is less the case for Southeast Australia, where RFI probabilities are very low, and open water fractions restricted. Note also that dynamic vegetation parameters, instead of the static FFO, could be used. One example would be to include the vegetation optical depth that is dynamically retrieved by SMOS. However, this study uses the static FFO, as the retrieved optical depth from SMOS is known to show strong oscillations which are not always justified (Kerr et al., 2012; Jackson et al., 2012).

Fig. 3(b) shows the 2010 mean soil moisture observation error for the SMOS grid in the Murray Darling Basin. It demonstrates that the observation error was generally smaller than the forecast error. This was chosen by design, as the observations are provided at coarser spatial scale (25 km) compared to the model grid (0.125°), which reduces the errors. Due to the nature of the observation error model, the spatial variability in the observation error is mainly driven by forest cover. Therefore, larger errors were encountered in the forested areas in the Southeast of the basin. Correspondingly, Fig. 3(c) shows the 2010 mean Kalman Gain for the first layer soil moisture content. The Kalman Gain weighs the forecast and observation errors, and represents the magnitude of the assimilation updates. The basin-averaged Kalman Gain equalled 0.32. Over time, the gain varied with the soil moisture conditions. Relatively higher values were associated with wet conditions, which relates to the multiplicative perturbation of the precipitation forcing (data not shown).

The observation error presented in Eq. (18) was only used directly for the case that the SM observations were rescaled to the model simulations according to their first order moment. In case of second or higher order rescaling of the observations, the observation error was rescaled according to:

$$\sigma_R^* = \frac{\sigma_{\mathrm{sim}}}{\sigma_{\mathrm{obs}}} \sigma_R, \tag{19}$$

where σ_R^* is the rescaled observation error standard deviation and σ_{sim} and σ_{obs} are the standard deviations of the SM simulations and observations, respectively.

2.5. Performance metrics

The evaluation of the model and data assimilation performance is based on a number of metrics. The model calibration is evaluated based on the Pearson correlation coefficient (R), the ratio of the mean (the mean of the simulations divided by the mean of the observations), the ratio of the standard deviation (the standard deviation of the simulations divided by the standard deviation of the observations), and the Kling Gupta Efficiency (KGE, Eq. (2)), which is a combined measure of the three previous metrics.

The impact of the assimilation experiments on the soil moisture simulations is assessed based on the correlation coefficient (R), the bias (m^3/m^3), the root mean square error (RMSE, m^3/m^3) and the efficiency index (EFF, %) (Aubert, Loumagne, & Oudin, 2003; Brocca et al., 2010, 2012):

$$\mathrm{EFF} = 100\left[1 - \frac{\sum_t \left(X_{\mathrm{sim_{DA}}}(t) - X_{\mathrm{obs}}(t)\right)^2}{\sum_t \left(X_{\mathrm{sim_{OL}}}(t) - X_{\mathrm{obs}}(t)\right)^2}\right], \tag{20}$$

with t the time, X_{obs} the observed quantity, and $X_{\mathrm{sim_{OL}}}$ and $X_{\mathrm{sim_{DA}}}$ the simulated quantities without (OL) and with (DA) data assimilation, respectively. If EFF is greater than zero, the assimilation improves the performance of the simulations.

The evaluation of the streamflow simulations is based on the same metrics used for the soil moisture evaluation, with the exception that the RMSE is normalized by the standard deviation of the observations (σ_{obs}) to account for differences between the scales of the sub-basins.

3. Results and discussion

3.1. Model calibration and validation

The VIC model was implemented for the Murray Darling Basin to perform simulations of soil moisture, runoff and baseflow on an hourly time step. A grid-based calibration of VIC was performed to match monthly observations of streamflow from 2005–2010 for the 169 unregulated gauge stations across the Murray Darling.

Fig. 4 shows the gridded calibration results for the two parameters which have the largest impact on surface runoff, i.e. the infiltration parameter b and the second layer thickness $dp2$. Note that the gridded parameter results only cover the total drainage area of the selected gauge stations, for which the performance of the calibration can be validated. The value of b is inversely related to the infiltration capacity, as given by Eq. (1). Therefore, higher values of b correspond with increased runoff sensitivity. Fig. 4(a) shows that high b-values mainly occur in the East of the basin, coinciding with the Australian Alps and Great Dividing Range, where large amounts of runoff are habitual. As revealed by Fig. 4(b), $dp2$ is largest in the drier Northwest of the basin. The $dp2$ parameter has a large impact on evaporation, as most of the vegetation roots are contained within the second soil layer. Therefore, larger values of $dp2$ facilitate increased evaporative losses to reduce the amount of runoff in the dry areas of the basin.

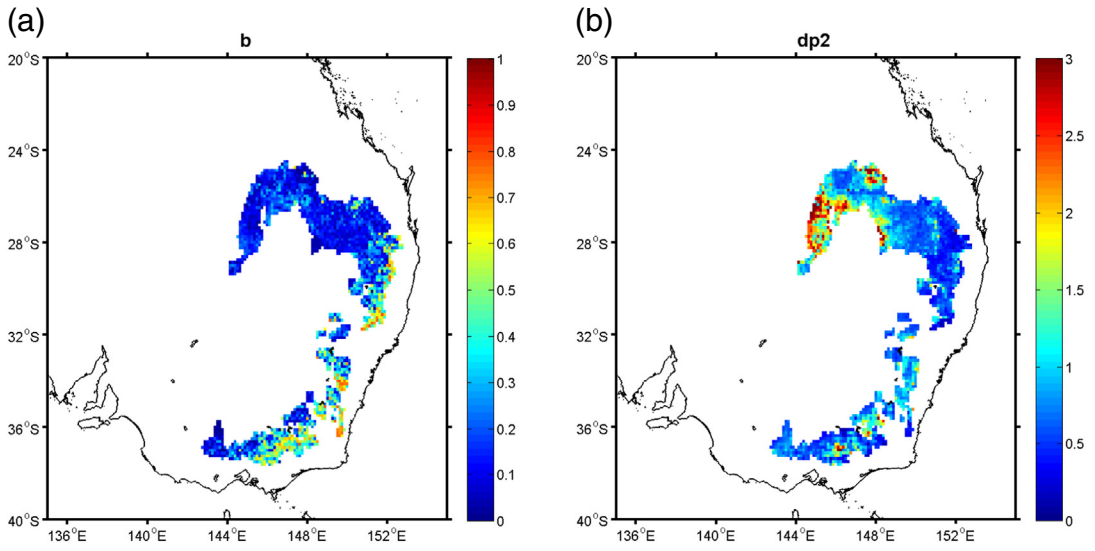

Fig. 4. The calibrated parameters for (a) *b* and (b) *dp2* over the total drainage area of the selected 169 gauge stations within the Murray Darling Basin.

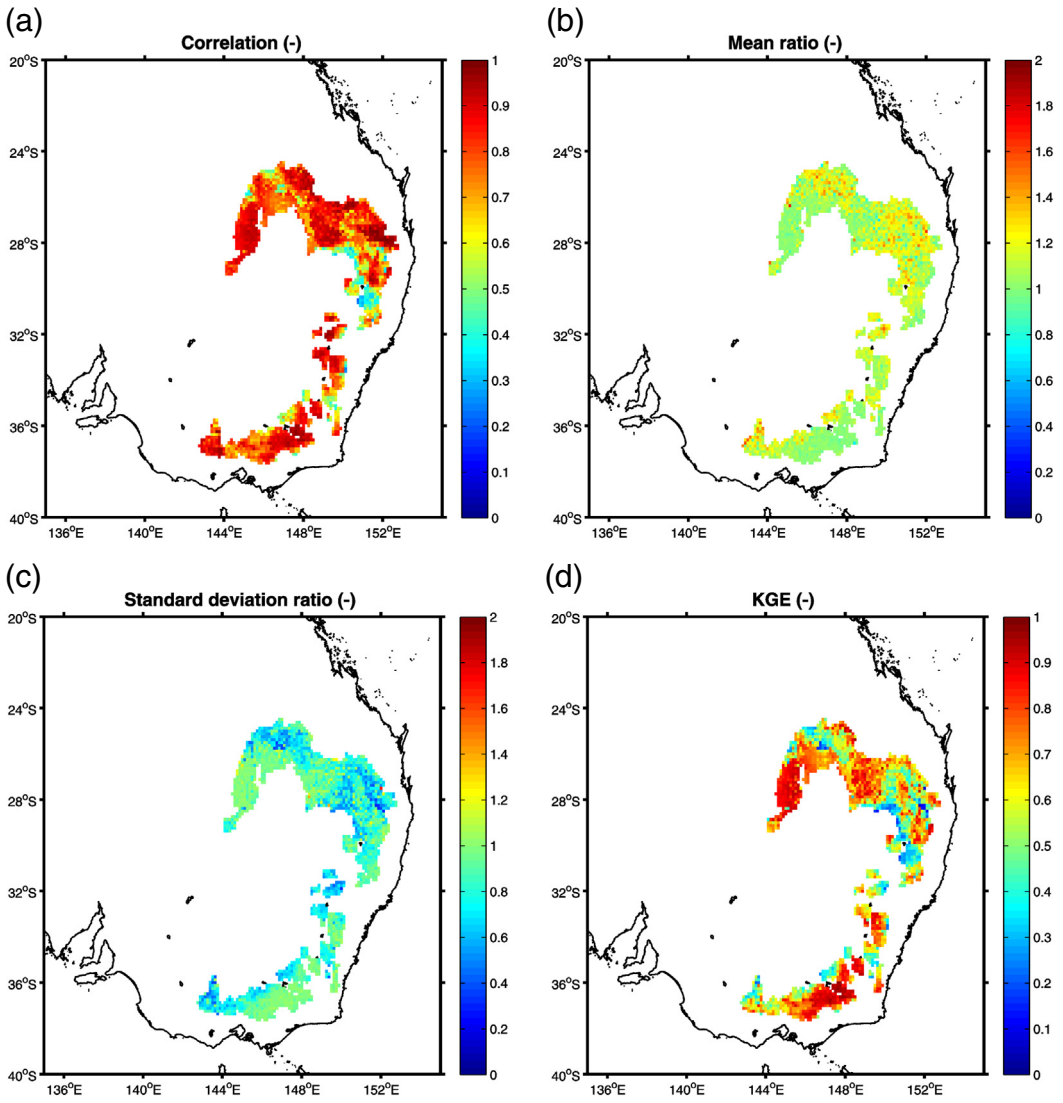

Fig. 5. Grid-based results of the calibration objective function (5 years, 2005–2010), with (a) the correlation, (b) the mean ratio, (c) the standard deviation ratio and (d) the Kling Gupta Efficiency (KGE).

Fig. 5 evaluates the optimized simulations on a monthly time scale for the period 2005–2010. The figure shows the different criteria in the calculation of the KGE, i.e. the correlation, the ratio of the mean, the ratio of the standard deviation, and the KGE itself. A high correlation (>0.7) is found for most grid cells, which may partly be explained through reproduction of the seasonal cycle by the simulations at monthly resolution. A slight overestimation of the mean ratio is noticeable, whereas the standard deviation ratio is slightly underestimated. Nevertheless, in general the monthly streamflow simulations correspond well to the observations, as supported by KGE values mostly in the range of 0.5–0.9. Only few grid cells have KGE values below 0.5. As discussed by Troy et al. (2008), performance decrement can occur in regions with low runoff ratios. In such areas, the monthly runoff volume may be in the same order as the error in precipitation, through which the calibration becomes very sensitive to errors in meteorological forcings. This may particularly occur for ephemeral streams in arid regions. Other reasons for decreased performance may relate to errors in the gauge observations and shortcomings in the calibration method, e.g. the assumption of constant runoff ratios throughout the catchments and monthly time scale.

3.2. Soil moisture analysis

A suite of data assimilation (DA) experiments was performed to assess whether coarse-scale SMOS SM retrievals can improve the finer-scale VIC simulations on the daily time scale. The focus was on the daily simulations to optimally exploit the high temporal observation frequency from SMOS. The time period for the analysis covered the years 2010–2011. The assimilation runs were compared to the open loop (OL, without assimilation) run which was performed in ensemble mode. Thereby, the forecast estimate referred to the ensemble mean, and the uncertainty to its standard deviation. The use of an ensemble mode for benchmarking the assimilation runs is advantageous as it reduces the effects of possible biases introduced by the model ensemble generation. Furthermore, the assimilation experiments distinguished between three methods for bias correction between the SMOS observations and model simulations. These are the rescaling of the first, first and second, and all order moments of the observed soil moisture distribution, which are referred to as DA-MEAN, DA-SD and DA-CDF, respectively.

As a first assessment, Fig. 6 displays a comparison of the mean soil moisture simulated by VIC and observed by SMOS, as well as their mean bias and temporal Spearman rank correlation, for the year 2010. Note that for this demonstration, the VIC simulations were cross-masked with the SMOS observations. It shows that VIC and SMOS revealed similar spatial patterns mainly in the North of the basin. Both fields also showed wet areas covering the center-North and center-South, where soil texture is characterized by high (±50%) clay contents. Disagreement was found for the evergreen broadleaved forests and mountainous areas in the South and East of the basin. However, both the VIC simulations and SMOS retrievals were characterized by a relatively larger uncertainty (Fig. 3) over these areas. The basin-averaged SM bias equaled 0.015 m^3/m^3 (VIC minus SMOS); however, regional biases were considerably larger, ranging from approximately −0.2 to 0.2 m^3/m^3. The correlation was larger than 0.5 for most areas in the basin, except for the Southeast, where spatial patterns were also in disagreement.

In a second assessment, the OL and DA predictions of soil moisture were compared to in situ measurements from OzNet and associated retrievals from SMOS. The analysis was performed for the 21 VIC cells covering in total 49 in situ stations (Section 2.1). Fig. 7 shows an example of this comparison for the cell comprising Yanco site 3 (Y3, latitude = −34.6208°, longitude = 146.4239°). For representation convenience, the hourly soil moisture simulations and in situ data were averaged to a daily time scale, whereas the SMOS observations were averaged over ascending (6 am) and descending (6 pm) orbits. Note that this averaging had a negligible effect on climatologies, as revealed by a comparison with hourly values (data not shown). Also note that the simulations are extracted at the fine scale, whereas SMOS observations are at the coarse scale. The figure shows that the OL predictions have a slightly reduced dynamic range compared to the Y3 data, which was also found for most of the other in situ stations. Although no strong conclusions can be drawn due to different representativeness, the reduced dynamic range of VIC has been reported previously by Pan, Sahoo, and Wood (2014) and was explained by its lack of built-in under-canopy soil evaporation, and its exponential decay of gravity drainage and plant transpiration with decreasing soil moisture. Conversely, the SMOS retrievals displayed a slightly larger dynamic range compared to the Y3 measurements. Consequently, the assimilation of SMOS retrievals (DA-MEAN) dilated the dynamic range of the model simulations and improved the correspondence with the in situ measurements. It should be remarked that the assimilation improvements may thus not only be related to corrections of random errors, but may also partly be caused by modification of the model climatology, i.e. dynamic range. A similar impact on the model climatology was observed previously by Draper et al. (2011) after the assimilation of ASCAT observations into SIM over France. Finally, Fig. 7 also demonstrates that the assimilation constraints the uncertainty associated with the soil moisture predictions.

Table 3 compares time series metrics, i.e. the bias (m^3/m^3), R (−) and RMSE (m^3/m^3) between the hourly VIC OL and DA simulations, the SMOS retrievals and OzNet measurements, averaged for the 21 grid cells. For the validation of SMOS, the in situ measurements were thinned to the time steps of the retrievals, yielding a significantly lower number of data points *n*. To (partly) remove the impact of representativeness, the metrics were also calculated after rescaling the VIC simulations and SMOS retrievals to the in situ measurements, through CDF-matching. Both the (non-rescaled) simulations and SMOS retrievals showed a small dry bias compared to the in situ data. The correlation of the SMOS retrievals exceeds the correlation of the OL, although the comparison may be affected by the different number of data points. The bias-unaware RMSE of both the OL (0.079 m^3/m^3) and SMOS (0.091 m^3/m^3) is relatively large, however, reduces considerably to 0.058 m^3/m^3 for OL and 0.045 m^3/m^3 for SMOS after rescaling. In conclusion, the statistics of Table 3 reveal that the SMOS retrievals generally show a larger correspondence with the in situ measurements compared to the OL simulations. They also underline the importance and impact of the rescaling, which aligns the climatologies of the data records to account for differences in representativeness.

In addition, Table 3 shows the time series statistics after the assimilation experiments with different bias correction methods. The largest improvements over the OL were achieved with DA-MEAN, increasing the correlation R-CDF from 0.564 to 0.714 and reducing the RMSE-CDF from 0.058 m^3/m^3 to 0.046 m^3/m^3. The efficiency EFF of the DA-MEAN assimilation equals almost 33%. The DA-SD and DA-CDF experiments show slightly less improvements, characterized by R-CDFs of approximately 0.69, RMSE-CDFs of 0.049 m^3/m^3 and EFFs close to 27%. The obtained improvements are in line with several other studies. After assimilating ASCAT observations, Matgen et al. (2012) observed efficiencies in the order of 5–10% depending on the magnitude of the observation error. Brocca et al. (2012) obtained efficiencies of 11% and 42% after assimilating ASCAT surface and root-zone soil moisture observations. Ridler, Madsen, Stisen, Bircher, and Fensholt (2014) noticed improvements in R^2 (from 0.718 to 0.807) and RMSE (from 0.022 to 0.020 m^3/m^3) through assimilation of SMOS retrievals. Finally, Renzullo et al. (2014) assimilated ASCAT and AMSR-E observations over Australia, which led to an increase in average correlation from 0.68 to 0.73 with respect to 0–30 cm in situ measurements of OzNet.

The slightly lower impact of DA-SD and DA-CDF can be explained by the more precise rescaling to the model climatology. As noted by Draper et al. (2011), a more stringent bias correction between the observations and the forecast model, e.g. as in DA-SD and DA-CDF compared to

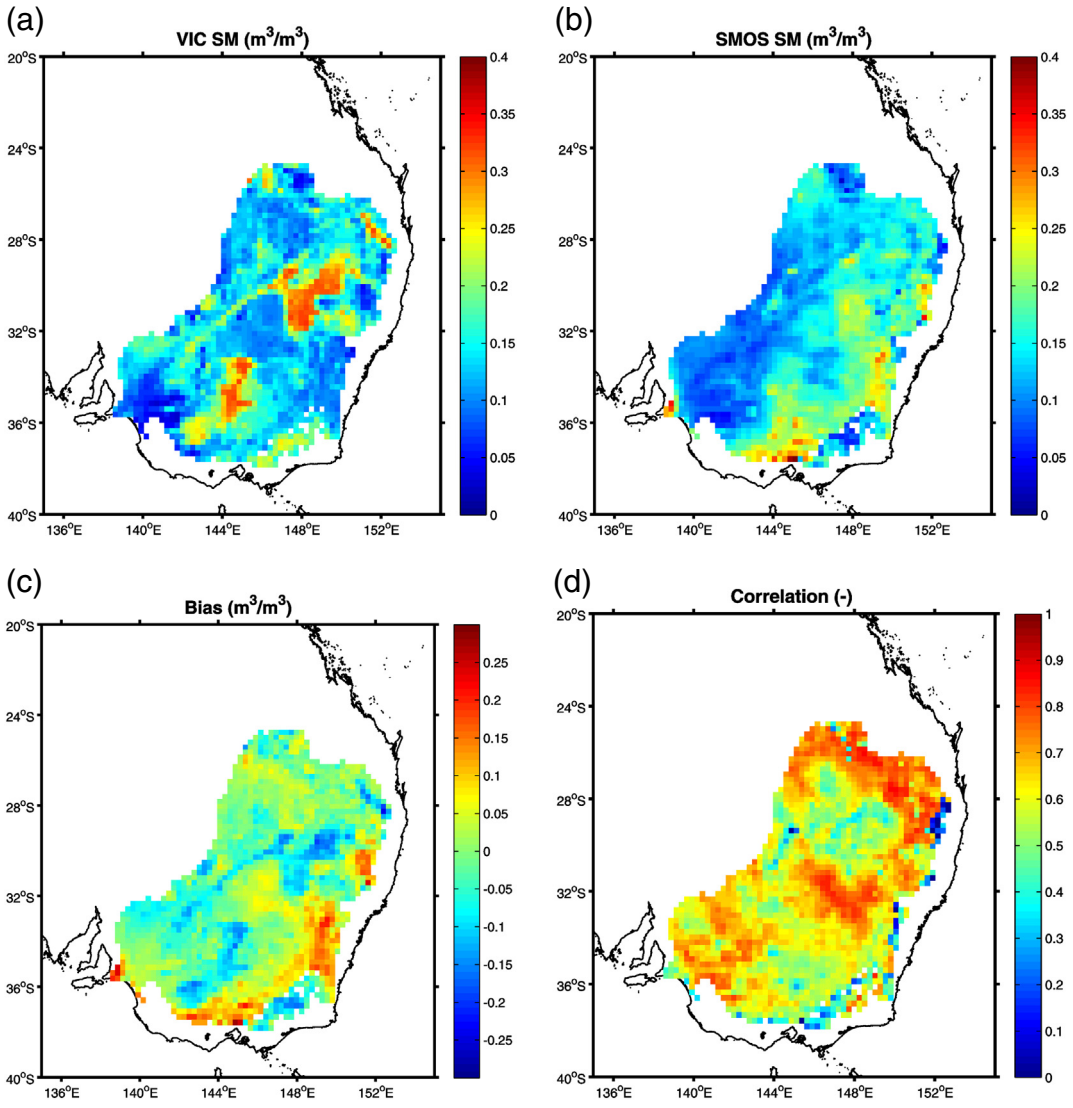

Fig. 6. The 2010 mean soil moisture (a) simulated by VIC and (b) observed by SMOS, with (c) the mean bias and (d) the Spearman rank correlation.

DA-MEAN, allows the assimilation to correct for errors which are not related to model climatology. Consequently, the improvement may be less pronounced, particularly if climatological differences are shown. However, it is also important to remark that the rescaling of the observational variability toward the model variability implies full trust in the dynamic range of the model, which is not always justified. Moreover, this may confine the more extreme wet and dry model predictions in the analysis. The latter can be sub-optimal for matching the in situ measurements, which mostly showed a larger variability than the OL simulations in this study. Finally, a last caveat to these results is that mainly the methods with rescaling of the variance, i.e. DA-SD and DA-CDF, may show sub-optimal performance due to the fact that they are based on a relatively short 2-year data record, whereas longer records are preferred for the rescaling of higher order moments. As mentioned in Section 2.4.4, further research on the use of alternative bias correction approaches that resolve these shortcomings is recommended.

3.2.1. Streamflow analysis

The open loop streamflow simulations are compared with measurements of the 169 selected gauge stations for the validation period of 2010–2011 through Taylor diagrams, presented in Fig. 8, on a monthly and daily time scale, respectively. Thereby, the standard deviations of the simulations are represented through their ratio over the standard deviations of the observations, and should ideally equal 1. Furthermore, the RMSE values for each station have been normalized by the corresponding standard deviation of the observations in order to avoid scale differences between the selected catchments. As shown in Fig. 8, the monthly simulations match the observations well. However, a decreased performance is observed for the daily simulations by all three metrics presented in the Taylor diagrams.

The relatively poor performance at the daily time scale may be related to the semi-arid character of the basin. As discussed by Alvarez-Garreton, Ryu, Western, Crow, and Robertson (2014), the semi-arid catchments within the Murray Darling Basin often show a dominant surface runoff, and a negligible baseflow component. The initial runoff generation is controlled by the antecedent soil moisture content. Thereby, rainfall does not result in measurable runoff when the catchment does not reach a threshold soil moisture level. However, rainfall may lead to large runoff generation after reaching this threshold. A particular challenge for the LSM is to correctly represent this saturation excess runoff process at a large spatial scale. More specifically for this study, low runoff observations may induce low values of the infiltration parameter *b* during calibration (Fig. 4). However, such low *b*-values may prevent the accurate simulation of runoff peak flows, through which the simulations underestimate streamflow variability, as revealed by Fig. 8. Another major contributor of the increased errors on the daily

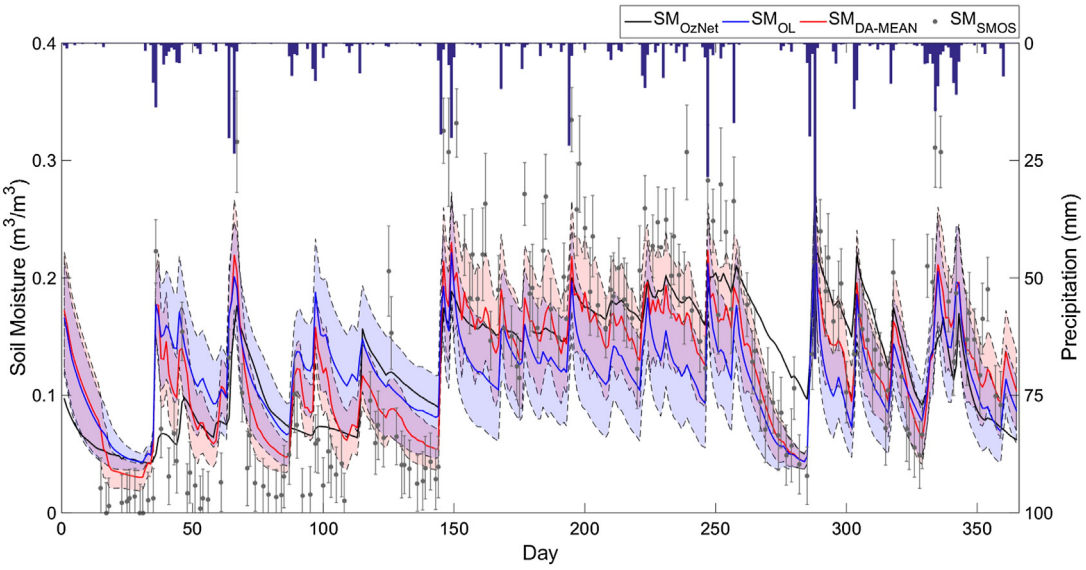

Fig. 7. Time series comparison between the daily soil moisture measurements at Yanco 3, the VIC open loop (OL) and data assimilation (DA-MEAN) simulations, and SMOS retrievals for 2010. The shaded areas represent the uncertainty (standard deviation) in the OL (blue) and DA-MEAN (red) simulations, whereas the error bars indicate the uncertainty (standard deviation) in the SMOS retrievals. (For interpretation of the references to color in this figure legend, the reader is referred to the web version of this article.)

scale are errors in precipitation. According to Alvarez-Garreton et al. (2014), the precipitation error may especially dominate the error in streamflow when the catchment has exceeded the soil moisture threshold at which runoff generation starts. Above this threshold, soil moisture has limited influence on the runoff volume. Finally, part of the increased errors may also be explained by the simplistic formulation of the routing model.

Fig. 8 also shows the performance of the monthly and daily streamflow simulations with the assimilation (DA-MEAN) of SM retrievals. For both time scales, the simulations showed improvements in correlation, normalized RMSE, and standard deviation ratio for most of the stations. However, few stations noticed an inflation of the standard deviation ratio. A possible reason therefore may be found in the introduction of biases in streamflow, notwithstanding the assimilated soil moisture retrievals were corrected for biases a priori.

A comparison of the assimilation improvements between different bias correction methods is presented in Fig. 9, through histograms of R and normalized RMSE (nRMSE, with respect to the daily gauge measurements) for the OL and DA predictions and histograms of EFF. Improvements in Fig. 9 are depicted by a shift of the DA histogram to larger values for R and EFF and lower values for nRMSE. The corresponding mean statistics for the 169 gauge stations are shown in Table 4. As revealed by Fig. 9 and Table 4, the largest improvements were observed for DA-MEAN, with an increase in R from 0.607 to 0.654 and decrease in nRMSE from 0.813 to 0.784. DA-SD and DA-CDF moderately improved the streamflow simulations with an increase in R to 0.628 and 0.625, and decrease in nRMSE to 0.799 and 0.801, respectively. The EFF histogram for DA-MEAN is clearly left-skewed, with a larger frequency of positive values up to a maximum of 40%. Nevertheless, a considerable number of stations have an EFF-value close to zero, meaning that the assimilation has no impact on the simulation accuracy. Few stations also have negative EFF-values with deterioration of the results. The EFF histograms for DA-SD and DA-CDF have a less pronounced skew indicating less significant improvements. The magnitudes of improvements in streamflow simulation in this study are in line with literature. For example, Matgen et al. (2012) achieved an efficiency close to 10%, whereas an EFF-value of 40% was obtained by Brocca et al. (2012), both after the assimilation of ASCAT wetness observations.

It is important to note that the relative improvements in streamflow prediction for the different bias correction methods are consistent with their improvements in soil moisture. For both the simulation of soil moisture and streamflow, the optimal results in this study are obtained with DA-MEAN. This supports that improvements in antecedent soil moisture conditions through the assimilation of SMOS retrievals propagate to improvements in streamflow prediction. The better performance of DA-MEAN for streamflow simulation is more pronounced compared to the soil moisture analysis. This may be explained by the fact that the rescaling of second and higher order moments reduces the variability and extremes of the soil moisture retrievals, and consequently confines runoff peaks. Similar findings were obtained by Alvarez-Garreton et al. (2014). They concluded that the rescaling through linear regression resulted in underestimated peak soil moisture values, preventing the assimilation to correctly update runoff peaks. Peak predictions were better represented after CDF-matching the anomalies of the observations, which better preserved the soil moisture extremes.

Improvements in predictive skill of DA-MEAN were mostly apparent in the simulation of streamflow peak observations. This is supported by Fig. 10, which displays the RMSE ratio (RMSE of DA-MEAN over RMSE of OL) and EFF for rank percentiles of the streamflow records. More specifically, the rank percentile of 10% represents the 10% highest values of the streamflow records; the 100% rank percentile represents the entire record. It shows that the 10% rank percentile is characterized by the

Table 3
The performance metrics, i.e. root mean square error (RMSE, m^3/m^3), correlation (R), and efficiency (EFF, %), for the different soil moisture fields in comparison with in situ measurements of OzNet, averaged over all 49 stations, for the period of 2010–2011. The metrics denoted with -CDF are obtained after rescaling the fields through CDF-matching.

SM record	*n*	Bias	R	R-CDF	RMSE	RMSE-CDF	EFF	EFF-CDF
SMOS	369	−0.019	0.690	0.726	0.091	0.045	–	–
Open loop	10,604	−0.027	0.547	0.564	0.079	0.058	–	–
DA-MEAN	10,604	−0.033	0.701	0.714	0.076	0.046	5.648	32.719
DA-SD	10,604	−0.031	0.655	0.682	0.078	0.049	3.427	25.959
DA-CDF	10,604	−0.031	0.666	0.690	0.077	0.049	4.092	27.392

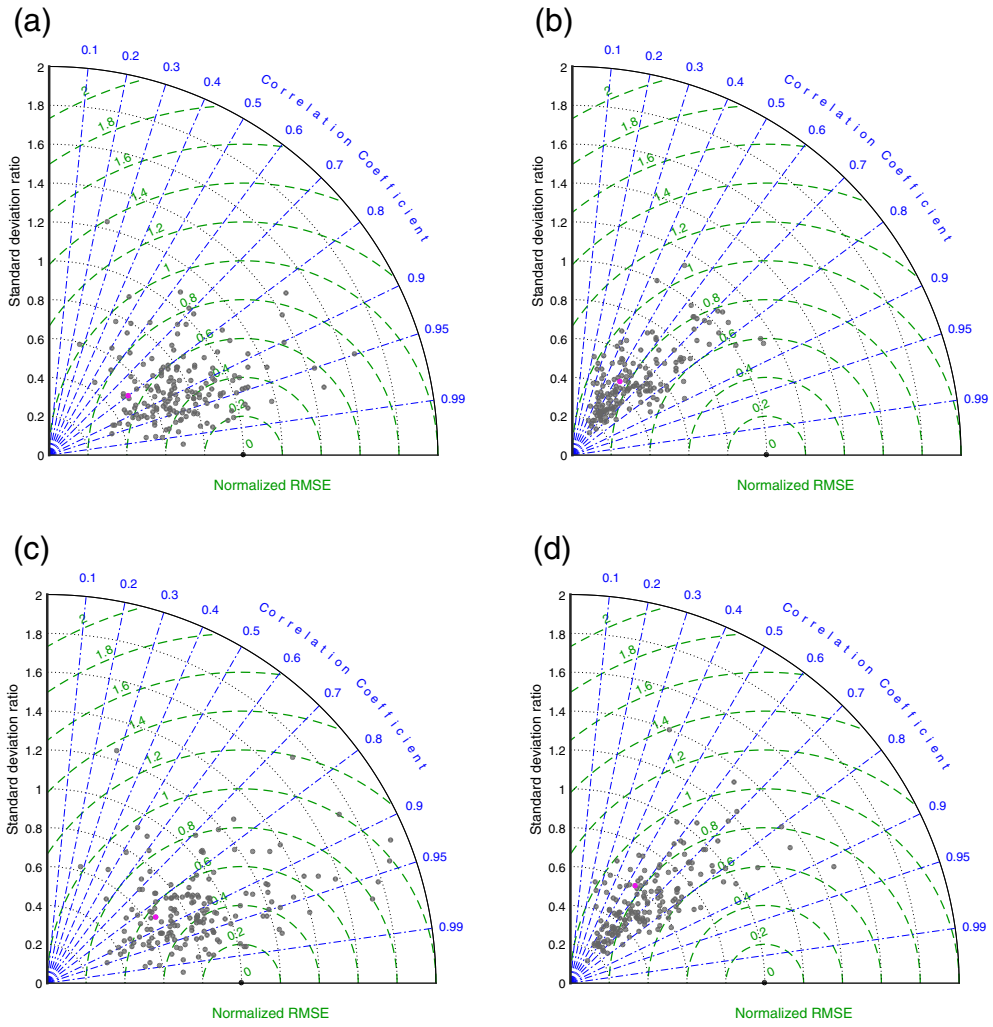

Fig. 8. Taylor diagrams comparing the simulations and observations of streamflow across all 169 gauges on a (a, c) monthly and (b, d) daily time step, during the 2-year period of 2010–2011. The top panel (a, b) shows the results for the open loop (OL), whereas the bottom panel (c, d) shows the results for the data assimilation (DA-MEAN). The reference (optimal) skill point is shown in black, and the focus gauge station at Seven Creeks in magenta.

lowest RMSE ratio and highest efficiency. Further, both metrics gradually decrement with increased percentiles. These findings are in agreement with Ridler et al. (2014), who observed improvements in peak discharge, although over-corrected, after assimilating SMOS retrievals over Western Denmark. In addition, Wanders et al. (2014) found that the assimilation of remotely sensed soil moisture observations improved the quality of flood alerts in the Upper Danube Basin in terms of timing and the exact height of the flood peak.

Finally, Fig. 11 shows an example comparison between the OL and DA-MEAN simulations and streamflow measurements for the gauge station at Seven Creeks (ID: 405234B, latitude: −36.8870°, longitude: 145.6828°, catchment area: 153 km^2). To improve clarity, only a subset of the 2010–2011 validation period is shown. The location of the station is marked in Fig. 1, whereas the performances of the OL and DA-MEAN simulations for this station are also highlighted in Fig. 8. As demonstrated by Fig. 11, the assimilation clearly improved runoff simulation. As can also be derived from this figure, the simulations are likely influenced by errors in the precipitation forcing. For instance, the large runoff peak observations at time steps 310 and 316 are associated with relatively low precipitation volumes, through which both events are missed out in the simulations. Additional errors are noticeably introduced by the routing model. For instance, the runoff peak observations at time steps 225 and 232 are well captured in terms of magnitude; however, the first peak simulation is one day early, whereas the second peak simulation lags one day behind. Clearly, these minor (one-day) timing errors may have profound impact on performance metrics. However, notwithstanding these limitations, the figure once again convincingly demonstrates that the assimilation of SMOS SM retrievals increases the accuracy of streamflow simulations.

4. Conclusions

The objective of this study was to assess the merit of assimilating SMOS SM observations for hydrologic model simulations, with a focus on soil moisture and streamflow in the Murray Darling Basin. Therefore, 49 in situ soil moisture stations across the Murrumbidgee sub-basin and 169 stream gauge stations across unregulated catchments were selected to evaluate improvements during data assimilation in VIC. The VIC model was first calibrated to match streamflow simulations with gauge measurements. While the calibrated model simulated the observed streamflow records with reasonable accuracy on a monthly basis, the simulation was poor at daily time scale. The larger errors at the daily time scale could be related to errors in the precipitation forcing, particularly as the precipitation field was sampled to a finer scale compared to its spatial resolution. Other aspects that may have contributed to increased errors are the simplicity of the routing model and perhaps inadvertent regulations.

A suite of SMOS SM data assimilation experiments were performed, with the aim to improve the initial soil moisture conditions and associated water fluxes, in particular surface runoff. The experiments were

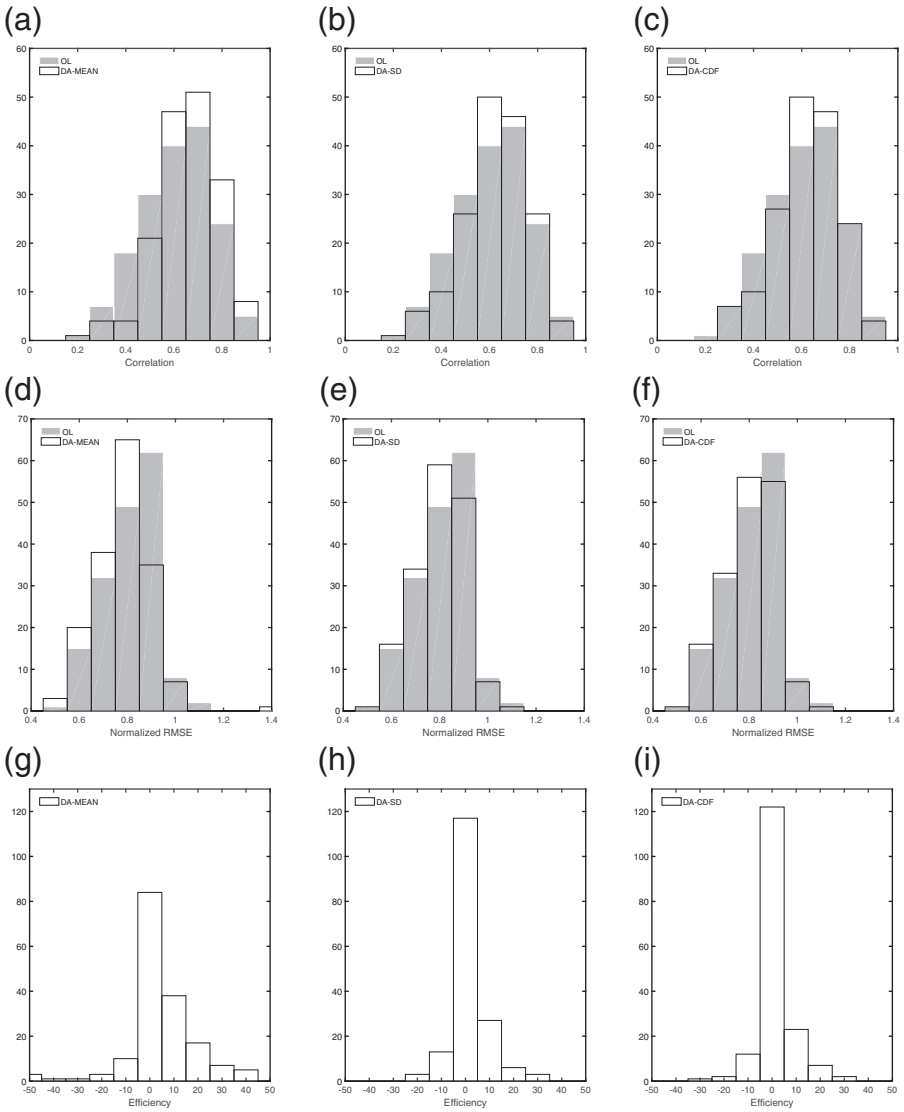

Fig. 9. Histograms showing the improvement of the (top) correlation and (middle) normalized RMSE in daily streamflow simulation across all 169 gauges, for the data assimilation experiments (left) DA-MEAN, (center) DA-SD and (right) DA-CDF, during the 2-year period of 2010–2011. The bottom panel shows the associated efficiencies of the DA experiments.

designed to investigate the effect of bias correction methods on the assimilation results. The bias correction methods distinguished between the rescaling of (1) the long term mean, (2) the mean and variance, and (3) the soil moisture distribution. A comparison to in situ soil moisture measurements from OzNet demonstrated that the rescaling of the variance and higher order moments provided sub-optimal results for this study. Rescaling of the observational variability to the dynamic range of the model implies full trust in the model range and may reduce the variability and extremes of the soil moisture retrievals. The most accurate bias correction method for this study was therefore the first order rescaling of the long term mean. Preserving the observational variability improved the variability of the assimilation results, and accordingly

Table 4
The performance metrics, i.e. normalized root mean square error (nRMSE), correlation (R), and efficiency (EFF, %), for the daily streamflow simulations in comparison with gauge measurements, averaged over all 169 stations, for the period of 2010–2011.

Model run	R	Normalized RMSE	EFF
Open loop	0.607	0.813	–
DA-MEAN	0.654	0.784	4.416
DA-SD	0.628	0.799	1.944
DA-CDF	0.625	0.801	1.505

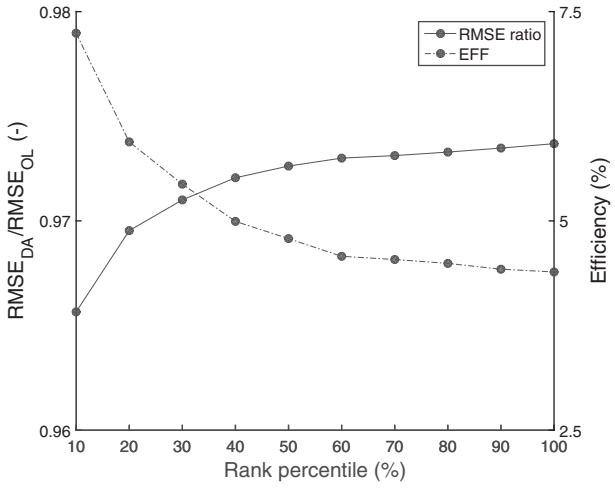

Fig. 10. The RMSE ratio and efficiency of the data assimilation (DA-MEAN) for subsets of ranked streamflow time series for the period of 2010–2011, averaged over all 169 gauge stations.

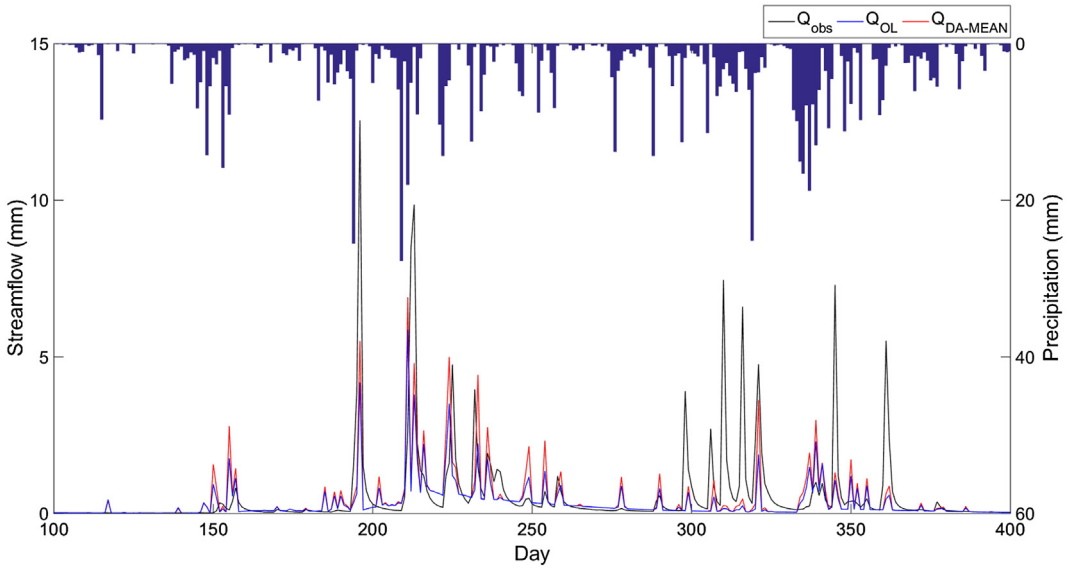

Fig. 11. Precipitation and streamflow time series, comparing the open loop (OL) and data assimilation (DA-MEAN) simulations with gauge measurements at Seven Creeks, for a subset of the 2010–2011 validation period.

decreased the RMSE from 0.058 to 0.046 m^3/m^3 and increased R from 0.564 to 0.714, averaged over all 49 OzNet stations. The efficiency of the assimilation was found to be 33%. However, it should be remarked that part of this improvement may be caused by a slight modification of the model climatology, whereas the main objective of data assimilation is to correct for random errors other than model climatology. Furthermore, the optimal correction method may be subject to the specific conditions of this study. Therefore, further research on the comparison of more comprehensive bias correction methods for a wide range of conditions is highly recommended.

The gross validation of the assimilation experiments was performed at the level of the streamflow simulations. For this purpose, simulations were compared to measurements of 169 gauge stations across the Murray Darling Basin. Consistent with the soil moisture analysis, an optimal performance was observed for bias correction of the long term mean, whereas rescaling of the variance or matching of distributions led to minor improvements only. The largest improvements were apparent in the simulation of peak runoff observations. This resulted from an improved characterization of the antecedent soil moisture conditions that control the generation of runoff. The improvement of peak runoff simulations is of particular importance for operational water management, which is often focused toward the forecasting of extreme events such as floods.

In conclusion, the assimilation of coarse-scale SMOS soil moisture retrievals was found to convincingly improve the finer-resolution VIC model simulations of soil moisture and streamflow over a large spatial domain. Therefore, this study provides strong encouragement for the use of SMOS data in operational water management.

Acknowledgment

The work has been performed in the framework of the ESA-STSE project 'SMOS + Hydrology Study' and was partly funded through project SR/00/302 ('Hydras+') financed by the Belgian Science Policy (BELSPO), and the CNES Terre, Océan, Surfaces Continentales, Atmosphère (TOSCA) program. Furthermore, we would like to acknowledge the Australian Bureau of Meteorology and the University of Melbourne (Andrew Western and colleagues) for the support in the provision of the streamflow and soil moisture data. We also would like to acknowledge the Jülich Supercomputing Center for granting computation time on JUROPA. Hans Lievens is a postdoctoral research fellow of the Research Foundation Flanders (FWO). Valentijn Pauwels is currently a Future Fellow funded by the Australian Research Council.

References

Al Bitar, A., Leroux, D., Kerr, Y. H., Merlin, O., Richaume, P., Sahoo, A., et al. (2012). Evaluation of SMOS soil moisture products over continental US using the SCAN/SNOTEL network. *IEEE Transactions on Geoscience and Remote Sensing, 50*, 1572–1586.

Albergel, C., de Rosnay, P., Gruhier, C., Sabater, J. M., Hasenauer, S., Isaksen, L., et al. (2012). Evaluation of remotely sensed and modelled soil moisture products using global ground-based in situ observations. *Remote Sensing of Environment, 118*, 215–226.

Alvarez-Garreton, C., Ryu, D., Western, A. W., Crow, W. T., & Robertson, D. E. (2014). The impacts of assimilating satellite soil moisture into a rainfallrunoff model in a semi-arid catchment. *Journal of Hydrology, 519*, 2763–2774.

Aubert, D., Loumagne, C., & Oudin, L. (2003). Sequential assimilation of soil moisture and streamflow data in a conceptual rainfall runoff model. *Journal of Hydrology, 280*, 145–161.

Best, M. J., Pryor, M., Clark, D. B., Rooney, G. G., Essery, R. L. H., Ménard, C. B., et al. (2011). The Joint UK Land Environment Simulator (JULES), model description, Part 1: Energy and water fluxes. *Geoscientific Model Development, 4*, 677–699.

Bircher, S., Skou, N., Jensen, K. H., Walker, J. P., & Rasmussen, L. (2012). A soil moisture and temperature network for SMOS validation in Western Denmark. *Hydrology and Earth System Sciences, 16*, 1445–1463.

Brocca, L., Melone, F., Moramarco, T., Wagner, W., Naeimi, V., Bartalis, Z., et al. (2010). Improving runoff prediction through the assimilation of the ASCAT soil moisture product. *Hydrology and Earth System Sciences, 14*, 1881–1893.

Brocca, L., Moramarco, T., Melone, F., Wagner, W., Hasenauer, S., & Hahn, S. (2012). Assimilation of surface- and root-zone ASCAT soil moisture products into rainfall-runoff modeling. *IEEE Transactions on Geoscience and Remote Sensing, 50*, 2542–2555.

Brooks, R. H., & Corey, A. T. (1964). Hydraulic properties of porous media. *Hydrology Papers, Colorado State University, 3*, 1–37.

Burke, E. J., Shuttleworth, W. J., Lee, K., & Bastidas, L. A. (2001). Using area-average remotely sensed surface soil moisture in multipatch land data assimilation systems. *IEEE Transactions on Geoscience and Remote Sensing, 39*, 2091–2100.

Chen, F., Crow, W. T., Starks, P. J., & Moriasi, D. N. (2011). Improving hydrologic predictions of a catchment model via assimilation of surface soil moisture. *Advances in Water Resources, 34*, 526–536.

Choudhury, B., Schmugge, T., Chang, A., & Newton, R. (1979). Effect of surface roughness on the microwave emission from moist soils. *Journal of Geophysical Research-Atmospheres, 84*, 5699–5706.

Clark, D. B., Mercado, L. M., Sitch, S., Jones, C. D., Gedney, N., Best, M. J., et al. (2011). The Joint UK Land Environment Simulator (JULES), model description, Part 2: Carbon fluxes and vegetation dynamics. *Geoscientific Model Development, 4*, 701–722.

Crow, W. T., Koster, R., Reichle, R., & Sharif, H. (2005). Relevance of time-varying and time-invariant retrieval error sources on the utility of spaceborne soil moisture products. *Geophysical Research Letters, 32*, L24405.

De Lannoy, G. J. M., Houser, P. R., Pauwels, V. R. N., & Verhoest, N. E. C. (2007). State and bias estimation for soil moisture profiles by an ensemble Kalman filter: Effect of assimilation depth and frequency. *Water Resources Research, 43*, W06401.

Dickinson, R. E., Henderson-Sellers, A., Kennedy, P. J., & Wilson, M. F. (1986). *Biosphere-atmosphere transfer scheme (BATS) for the NCAR community climate model*. Technical Report TN-275 + STR.

Draper, C., Mahfouf, J. F., Calvet, J. -C., Martin, E., & Wagner, W. (2011). Assimilation of ASCAT near-surface soil moisture into the SIM hydrological model over France. *Hydrology and Earth System Sciences*, *15*, 3829–3841.

Drusch, M., Wood, E. F., & Gao, H. (2005). Observation operators for the direct assimilation of TRMM microwave imager retrieved soil moisture. *Geophysical Research Letters*, *32*, L15403.

Duan, Q. Y., Sorooshian, S., & Gupta, V. K. (1992). Effective and efficient global optimization for conceptual rainfall-runoff models. *Water Resources Research*, *28*, 1015–1031.

Duan, Q. Y., Sorooshian, S., & Gupta, V. K. (1994). Optimal use of the SCE-UA global optimization method for calibrating watershed models. *Journal of Hydrology*, *158*, 265–284.

Dumedah, G., & Walker, J. P. (2014). Intercomparison of the JULES and CABLE land surface models through assimilation of remotely sensed soil moisture in southeast Australia. *Advances in Water Resources*, *74*, 231–244.

Dumedah, G., Walker, J. P., & Rüdiger, C. (2014). Can SMOS data be used directly on the 15-km Discrete Global Grid. *IEEE Transactions on Geoscience and Remote Sensing*, *52*, 2538–2544.

Entekhabi, D., Njoku, E. G., O'Neill, P. E., Kellogg, K. H., Crow, W. T., Edelstein, W. N., et al. (2010). The soil moisture active passive (SMAP) mission. *Proceedings of the IEEE*, *98*, 704–716.

Escorihuela, M. J., Chanzy, A., Wigneron, J. P., & Kerr, Y. H. (2010). Effective soil moisture sampling depth of L-band radiometry: A case study. *Remote Sensing of Environment*, *114*, 995–1001.

Evensen, G. (1994). Sequential data assimilation with a nonlinear quasi-geostrophic model using Monte Carlo methods to forecast error statistics. *Journal of Geophysical Research, Oceans*, *99*, 10143–10162.

Gupta, H. V., Kling, H., Yilmaz, K. K., & Martinez, G. F. (2009). Decomposition of the mean squared error and NSE performance criteria: Implications for improving hydrological modelling. *Journal of Hydrology*, *377*, 80–91.

Hansen, M., Defries, R., Townshend, J., & Sohlberg, R. (2000). Global land cover classification at 1 km spatial resolution using a classification tree approach. *International Journal of Remote Sensing*, *21*, 1331–1364.

Houser, P., Shuttleworth, W. J., Famiglietti, J. S., Gupta, H. V., Syed, K. H., & Goodrich, D. C. (1998). Integration of soil moisture remote sensing and hydrologic modeling using data assimilation. *Water Resources Research*, *34*, 3405–3420.

Imaoka, K., Kachi, M., Fujii, H., Murakami, H., Hori, M., Ono, A., et al. (2010). Global change observation mission (GCOM) for monitoring carbon, water cycles, and climate change. *Proceedings of the IEEE*, *98*, 717–734.

Jackson, T. J., Bindlish, R., Cosh, M. H., Zhao, T., Starks, P. J., Bosch, D. D., et al. (2012). Validation of soil moisture and ocean salinity (SMOS) soil moisture over watershed networks in the U.S. *IEEE Transactions on Geoscience and Remote Sensing*, *50*, 1530–1543.

Jacquette, E., Al Bitar, A., Mialon, A., Kerr, Y., Quesney, A., Cabot, F., et al. (2010). SMOS CATDS level 3 global products over land. In C. M. U. Neale, & A. Maltese (Eds.), *Remote Sensing for Agriculture, Ecosystems, and Hydrology XII. volume 7824 of Proceedings of SPIE-The International Society for Optical Engineering. Conference on Remote Sensing for Agriculture, Ecosystems, and Hydrology XII, Toulouse, France*.

Jones, D. A., Wang, W., & Fawcett, R. (2009). High-quality spatial climate data-sets for Australia. *Australian Meteorological and Oceanographic Journal*, *58*, 233–248.

Kerr, Y. H., Waldteufel, P., Richaume, P., Davenport, I., Ferrazzoli, P., & Wigneron, J. P. (2011). *Algorithm theoretical basis document (ATBD) for the SMOS level 2 soil moisture processor*. Technical Report SO-TN-ESL-SM-GS-0001 SM-ESL (CBSA) Toulouse.

Kerr, Y. H., Waldteufel, P., Richaume, P., Wigneron, J. P., Ferrazzoli, P., Mahmoodi, A., et al. (2012). The SMOS soil moisture retrieval algorithm. *IEEE Transactions on Geoscience and Remote Sensing*, *50*, 1384–1403.

Kerr, Y. H., Waldteufel, P., Wigneron, J. P., Martinuzzi, J. M., Font, J., & Berger, M. (2001). Soil moisture retrieval from space: The soil moisture and ocean salinity (SMOS) mission. *IEEE Transactions on Geoscience and Remote Sensing*, *39*, 1729–1735.

Knyazikhin, Y., Glassy, J., Privette, J. L., Tian, Y., Lotsch, A., Zhang, Y., et al. (1999). *MODIS leaf area index (LAI) and fraction of photosynthetically active radiation absorbed by vegetation (FPAR) product (MOD15) algorithm theoretical basis document*. Technical Report.

Koster, R. D., Guo, Z., Yang, R., Dirmeyer, P. A., Mitchell, K., & Puma, M. J. (2009). On the nature of soil moisture in land surface models. *Journal of Climate*, *22*, 4322–4335.

Kumar, S. V., Reichle, R. H., Harrison, K. W., Peters-Lidard, C. D., Yatheendradas, S., & Santanello, J. A. (2012). A comparison of methods for a priori bias correction in soil moisture data assimilation. *Water Resources Research*, *48*, W07523.

Lahoz, W. A., & De Lannoy, G. J. M. (2014). Closing the gaps in our knowledge of the hydrological cycle over land: Conceptual problems. *Surveys in Geophysics*, *35*, 623–660.

Lawrence, D. M., Oleson, K. W., Flanner, M. G., Thornton, P. E., Swenson, S. C., Lawrence, P. J., et al. (2011). Parameterization improvements and functional and structural advances in version 4 of the community land model. *Journal of Advances in Modeling Earth Systems*, *3* (M03001).

Lehner, B., Verdin, K., & Jarvis, A. (2006). *HydroSHEDS technical documentation*. Technical Report World Wildlife Fund US Washington, DC.

Leroux, D. J., Kerr, Y. H., Al Bitar, A., Bindlish, R., Jackson, T. J., Berthelot, B., et al. (2014). Comparison between SMOS, VUA, ASCAT, and ECMWF soil moisture products over four watersheds in US. *IEEE Transactions on Geoscience and Remote Sensing*, *52*, 1562–1571.

Leroux, D. J., Kerr, Y. H., Richaume, P., & Fieuzal, R. (2013). Spatial distribution and possible sources of SMOS errors at the global scale. *Remote Sensing of Environment*, *133*, 240–250.

Li, F., Crow, W. T., & Kustas, W. P. (2010). Towards the estimation of root-zone soil moisture via the simultaneous assimilation of thermal and microwave soil moisture retrievals. *Advances in Water Resources*, *33*, 201–214.

Li, H., Sheffield, J., & Wood, E. F. (2010). Bias correction of monthly precipitation and temperature fields from Intergovernmental Panel on Climate Change AR4 models using equidistant quantile matching. *Journal of Geophysical Research-Atmospheres*, *115*, D10101.

Liang, X., Lettenmaier, D., Wood, E., & Burges, S. (1994). A simple hydrologically based model of land-surface water and energy fluxes for general-circulation models. *Journal of Geophysical Research-Atmospheres*, *99*, 14415–14428.

Liang, X., Wood, E., & Lettenmaier, D. (1996). Surface soil moisture parameterization of the VIC-2 L model: Evaluation and modification. *Global and Planetary Change*, *13*, 195–206.

Liang, X., Wood, E., & Lettenmaier, D. (1999). Modeling ground heat flux in land surface parameterization schemes. *Journal of Geophysical Research-Atmospheres*, *104*, 9581–9600.

Lievens, H., Al Bitar, A., Verhoest, N. E. C., Cabot, F., De Lannoy, G. J. M., Drusch, M., et al. (2015). Optimization of a radiative transfer forward operator for simulating SMOS brightness temperatures over the Upper Mississippi Basin, USA. *Journal of Hydrometeorology*, *16*(3), 1109–1134.

Martens, B., Lievens, H., Colliander, A., Jackson, T. J., & Verhoest, N. E. C. (2015). Estimating effective roughness parameters of the L-MEB model for soil moisture retrieval using passive microwave observations from SMAPVEX12. *IEEE Transactions on Geoscience and Remote Sensing*, *53*(7), 4091–4103.

Masson, V., Moigne, P. L., Martin, E., Faroux, S., Alias, A., Alkama, R., et al. (2013). The SURFEXv7.2 land and ocean surface platform for coupled or offline simulation of earth surface variables and fluxes. *Geoscientific Model Development*, *6*, 929–960.

Matgen, P., Fenicia, F., Heitz, S., Plaza, D., de Keyser, R., Pauwels, V. R. N., et al. (2012). Can ASCAT-derived soil wetness indices reduce predictive uncertainty in well-gauged areas? A comparison with in situ observed soil moisture in an assimilation application. *Advances in Water Resources*, *44*, 49–65.

Maurer, E., O'Donnell, G., Lettenmaier, D., & Roads, J. (2001). Evaluation of the land surface water budget in NCEP/NCAR and NCEP/DOE reanalyses using an off-line hydrologic model. *Journal of Geophysical Research-Atmospheres*, *106*, 17841–17862.

McKenzie, N. J., Jacquier, D. W., Maschmedt, D. J., Griffin, E. A., & Brough, D. M. (2012). *The Australian soil resource information system (ASRIS) technical specifications*. Technical Report Revised Version 1.6 The Australian Collaborative Land Evaluation Program.

Merlin, O., Al Bitar, A., Walker, J., & Kerr, Y. (2010). An improved algorithm for disaggregating microwave-derived soil moisture based on red, near-infrared and thermal-infrared data. *Remote Sensing of Environment*, *114*, 2305–2316.

Nijssen, B., Schnur, R., & Lettenmaier, D. (2001). Global retrospective estimation of soil moisture using the variable infiltration capacity land surface model, 1980–93. *Journal of Climate*, *14*, 1790–1808.

Njoku, E. G., Jackson, T. J., Lakshmi, V., Chan, T. K., & Nghiem, S. V. (2003). Soil moisture retrieval from AMSR-E. *IEEE Transactions on Geoscience and Remote Sensing*, *41*, 215–229.

Pan, M., Sahoo, A., & Wood, E. F. (2014). Improving soil moisture retrievals from a physically-based radiative transfer model. *Remote Sensing of Environment*, *140*, 130–140.

Panciera, R., Walker, J. P., & Merlin, O. (2009). Improved understanding of soil surface roughness parameterization for L-band passive microwave soil moisture retrieval. *IEEE Geoscience and Remote Sensing Letters*, *6*, 625–629.

Parrens, M., Calvet, J. C., de Rosnay, P., & Decharme, B. (2014). Benchmarking of L-band soil microwave emission models. *Remote Sensing of Environment*, *140*, 407–419.

Pauwels, V. R. N., & De Lannoy, G. J. M. (2009). Ensemble-based assimilation of discharge into rainfall-runoff models: a comparison of approaches to mapping observational information to state space. *Water Resources Research*, *8*, W08428.

Pauwels, V. R. N., De Lannoy, G. J. M., Hendricks Franssen, H. -J., & Vereecken, H. (2013). Simultaneous estimation of model state variables and observation and forecast biases using a two-stage hybrid Kalman filter. *Hydrology and Earth System Sciences*, *17*, 3499–3521.

Pauwels, V. R. N., Hoeben, R., Verhoest, N. E. C., & De Troch, F. P. (2001). The importance of the spatial patterns of remotely sensed soil moisture in the improvement of discharge predictions for small-scale basins through data assimilation. *Journal of Hydrology*, *251*, 88–102.

Pauwels, V. R. N., Hoeben, R., Verhoest, N. E. C., De Troch, F. P., & Troch, P. A. (2002). Improvement of TOPLATS-based discharge predictions through assimilation of ERS-based remotely sensed soil moisture values. *Hydrological Processes*, *16*, 995–1013.

Rahmoune, R., Ferrazzoli, P., Kerr, Y. H., & Richaume, P. (2013). SMOS Level 2 retrieval algorithm over forests: Description and generation of global maps. *IEEE Journal of Selected Topics in Applied Earth Observations and Remote Sensing*, *6*, 1430–1439.

Reichle, R., & Koster, R. D. (2003). Assessing the impact of horizontal error correlations in background fields on soil moisture estimation. *Journal of Hydrometeorology*, *4*, 1229–1242.

Reichle, R., & Koster, R. D. (2004). Bias reduction in short records of satellite soil moisture. *Geophysical Research Letters*, *31*, L19501.

Reichle, R., Koster, R. D., Dong, J., & Berg, A. (2004). Global soil moisture from satellite observations, land surface models, and ground data: Implications for data assimilation. *Journal of Hydrometeorology*, *5*, 430–442.

Renzullo, L. J., van Dijk, A. I. J. M., Perraud, J. -M., Collins, D., Henderson, B., Jin, H., et al. (2014). Continental satellite soil moisture data assimilation improves root-zone moisture analysis for water resources assessment. *Journal of Hydrology*, *519*, 2747–2762.

Ridler, M. -E., Madsen, H., Stisen, S., Bircher, S., & Fensholt, R. (2014). Assimilation of SMOS-derived soil moisture in a fully integrated hydrological and soil-vegetation-atmosphere transfer model in Western Denmark. *Water Resources Research*, *50*, 8962–8981.

Rienecker, M. M., Suarez, M. J., Gelaro, R., Todling, R., Bacmeister, J., Liu, E., et al. (2011). MERRA - NASA's modern-era retrospective analysis for research and applications. *Journal of Climate*, *24*, 3624–3648.

Sabater, J. M., De Rosnay, P., & Balsamo, G. (2011). Sensitivity of L-band NWP forward modelling to soil roughness. *International Journal of Remote Sensing*, *32*, 5607–5620.

Sahoo, A. K., De Lannoy, G. J. M., Reichle, R. H., & Houser, P. R. (2013). Assimilation and downscaling of satellite observed soil moisture over the Little River Experimental Watershed in Georgia, USA. *Advances in Water Research*, *52*, 19–33.

Sheffield, J., Pan, M., Wood, E., Mitchell, K., Houser, P., Schaake, J., et al. (2003). Snow process modeling in the North American Land Data Assimilation System (NLDAS): 1. Evaluation of model-simulated snow cover extent. *Journal of Geophysical Research-Atmospheres*, *108*, 8849.

Sheffield, J., & Wood, E. F. (2008). Global trends and variability in soil moisture and drought characteristics, 1950–2000, from observation-driven simulations of the terrestrial hydrologic cycle. *Journal of Climate*, *21*, 432–458.

Smith, A. B., Walker, J. P., Western, A. W., Young, R. I., Ellett, K. M., Pipunic, R. C., et al. (2012). The Murrumbidgee soil moisture monitoring network data set. *Water Resources Research*, *48*, W07701.

Su, C. -H., & Ryu, D. (2015). Multi-scale analysis of bias correction of soil moisture. *Hydrology and Earth System Sciences*, *19*, 17–31.

Su, C. -H., Ryu, D., Crow, W. T., & Western, A. W. (2014). Beyond triple collocation: Applications to soil moisture monitoring. *Journal of Geophysical Research-Atmospheres*, *119*, 6419–6439.

Su, C. -H., Ryu, D., Young, R. I., Western, A. W., & Wagner, W. (2013). Inter-comparison of microwave satellite soil moisture retrievals over the Murrumbidgee Basin, southeast Australia. *Remote Sensing of Environment*, *134*, 1–11.

Troy, T. J., Wood, E. F., & Sheffield, J. (2008). An efficient calibration method for continental-scale land surface modeling. *Water Resources Research*, *44*, W09411.

Verhoest, N. E. C., van den Berg, M. J., Martens, B., Lievens, H., Wood, E. F., Pan, M., et al. (2015). Copula-based downscaling of coarse-scale soil moisture observations with implicit bias correction. *IEEE Transactions on Geoscience and Remote Sensing*, *53*(6), 3507–3521.

Wagner, W., Hah, S., Kidd, R., Melzer, T., Bartalis, Z., Hasenauer, S., et al. (2013). The ASCAT soil moisture product: A review of its specifications, validation results, and emerging applications. *Meteorologische Zeitschrift*, *22*, 5–33.

Walker, J., Willgoose, G., & Kalma, J. (2001). One-dimensional soil moisture profile retrieval by assimilation of near-surface observations: a comparison of retrieval algorithms. *Advances in Water Resources*, *24*, 631–650.

Wanders, N., Karssenberg, D., de Roo, A., de Jong, S. M., & Bierkens, M. F. P. (2014). The suitability of remotely sensed soil moisture for improving operational flood forecasting. *Hydrology and Earth System Sciences*, *18*, 2343–2357.

Wang, J. R., Oneil, P. E., Jackson, T. J., & Engman, E. T. (1983). Multifrequency measurements of the effects of soil moisture, soil texture and surface roughness. *IEEE Transactions on Geoscience and Remote Sensing*, *21*, 44–51.

Wigneron, J. P., Parde, M., Waldteufel, P., Chanzy, A., Kerr, Y. H., Schmidl, S., et al. (2004). Characterizing the dependence of vegetation model parameters on crop structure, incidence angle, and polarization at L-band. *IEEE Transactions on Geoscience and Remote Sensing*, *42*, 416–425.

Wilker, H., Drusch, M., Seuffert, G., & Simmer, C. (2006). Effects of the near-surface soil moisture profile on the assimilation of L-band microwave brightness temperature. *Journal of Hydrometeorology*, *7*, 433–442.

Wood, E. F., Roundy, J. K., Troy, T. J., van Beek, L. P. H., Bierkens, M. F. P., Blyth, E., et al. (2011). Hyperresolution global land surface modeling: Meeting a grand challenge for monitoring earth's terrestrial water. *Water Resources Research*, *47*, W05301.

Yilmaz, M. T., & Crow, W. T. (2013). The optimality of potential rescaling approaches in land data assimilation. *Journal of Hydrometeorology*, *14*, 650–660.

Zhao, R. -J., Zang, Y. -L., Fang, L. -R., Liu, X. -R., & Zhang, Q. -S. (1980). The Xinanjiang model. *Hydrological Forecasting Proceedings Oxford Symposium, IASH. 129*. (pp. 351–356).